EARTHQUAKE POTENTIAL OF THE EAST ANATOLIAN FAULT

by

Kaan Alper Uçan

B.S., Geological Engineering, Istanbul Technical University, 2017

Submitted to the Kandilli Observatory and Earthquake
Research Institute in partial fulfillment of
the requirements for the degree of
Master of Science

Graduate Program in Geodesy

Boğaziçi University

2020

ACKNOWLEDGEMENTS

Foremost, I would like to express my sincere gratitude and appreciation to Assoc. Prof. Fatih Bulut for having been my thesis supervisor, spending his invaluable time throughout this research. His guidance taught me how to carry out a research and present the results as clearly as possible. He helped me progress as a researcher with his guidance, experiences and patience during my thesis study. Without his support I would be lost in this thesis study.

I would also like to acknowledge my jury members; Assoc. Prof. Aslı Doğru, Prof. Cenk Yaltırak for spending their valuable time to evaluate this thesis.

I would like to express my gratitudes to the Department of Geodesy and special thanks to my colleagues Bengisu Gelin, Cansu Sevil Yıldırım for providing help and support during my master's thesis studies. This thesis has been supported by the research project "Slip deficit along Major Seismic Gaps in Turkey", which has been funded by Bogazici University (project number: 18T03SUP4).

I used the Steepest Descent Method developed by Dr. Rongjiang Wang and Generic Mapping Tools developed by Paul Wessel, Walter H. F. Smith, Remko Scharroo, Joaquim Luis and Florian Wobbe. I thank to the developers of these programs for letting many people use it freely.

I would also like to express my thanks to my sister, mom and dad for supporting me and providing emotional support whenever needed.

Last but not least, I would like to express my appreciation to my beloved friend for life Pelin Okutan for providing help, support and cheer for all the time during my education. She continuously encouraged me to continue my study and provided emotional support. I am grateful to her for being with me anytime I needed her.

ABSTRACT

EARTHQUAKE POTENTIAL OF THE EAST ANATOLIAN FAULT

This study aims to forecast magnitude of future strong (6.0≤ M <7.0) and major (7.0≤ M <8.0) earthquakes along the East Anatolian Fault Zone (EAFZ hereafter), which is a seismically active plate boundary between Arabian and Anatolian plates. In this context, we investigated segmentation of the EAFZ reviewing previous studies on structural variation zone and historical earthquakes. We analysed the combined GPS velocity field to obtain back-slips using steepest descent/gradient inversion method. The method projects GPS-derived back-slip rates onto the fault plane using Okada's quasi-infinite space model simulating elastic Green's functions to obtain on-fault slip deficit rates. Resulting slip deficit rates are used to estimate present-day slip budgets on each fault segment. We also analysed along-fault b-value distribution to verify if it can be used to differentiate between locked and creeping patches. Our results show that the EAFZ currently have a 1.51 m average slip. We suggest that the EAFZ is split into eight fault segments generating strong/major earthquakes. The January 24, 2020 Elazığ earthquake (M 6.8) ruptured the Sivrice-Pütürge segment verifying our segmentation model and magnitude forecasts for future earthquakes. We found no slip deficit accumulation observed on the Hacılar segment. Remaining six segments are able to generate three strong, three major earthquakes. Currently Karlıova, Kaleönü-Beyhan, Palu-Sivrice, Taştepe, Çelikhan-Erkenek, Gölbaşı-Pazarcık segments can currently generate M 7.0, M 6.9, M 7.1, M 6.8, M 6.9, M 7.4 earthquakes, respectively. Karlıova, Palu-Sivrice, Taştepe, Gölbaşı-Pazarcık segments currently have the potential to generate previous strong/major earthquakes they hosted. We observed a reverse correlation between slip deficit rates and b-values verifying that b-value can be used to discriminate locked and creeping fault segments.

ÖZET

DOĞU ANADOLU FAYI DEPREM POTANSİYELİ

Bu çalışmanın amacı, Arap ve Anadolu plakaları arasında sismik bir plaka sınırı olan Doğu Anadolu Fayı (DAF) boyunca gerçekleşebilecek olan orta (6.0≤ M <7.0) ve büyük (7.0≤ M <8.0) deprem potansiyellerini hesaplamaktır. Bu doğrultuda DAF yapısal özellikleri ve tarihsel depremleri üzerine yapılan önceki çalışmalardan faydalanarak segment yapısı incelendi. Green işlevleri simülasyonu ile Okada'nın yarı sonsuz uzay modelini kullanarak GPS'den türetilen back-slip oranlarını fay düzlemine kayma eksikliği olarak yansıtan "Steepest descent/gradient inversion" metodu kullanılarak back-slip değerlerini elde etmek için birleştirilmiş GPS hız alanı analiz edildi. Elde edilen kayma eksikliği oranları, her fay segmenti için günümüze kadar olan kayma eksikliği birikmesini hesaplamak için kullanılır. Ayrıca, kilitli ve krip yapan parçalar arasında ayrım yapmak için b-değeri dağılımının kullanılıp kullanılamayacağı fay boyunca analiz edildi. Sonuçlar DAF'ın günümüzde ortalama 1,51 metrelik bir kayma eksikliğine sahip olduğunu göstermektedir. Çalışmaya göre DAF orta ve büyük depremler oluşturan sekiz fay segmentinden oluşmaktadır. 24 Ocak 2020'de gerçekleşen Elazığ depremi (M 6.8) Sivrice-Pütürge segmentini kırarak bu çalışmadaki segment modelini ve gelecek depremler için büyüklük varsayımını doğruladı. Hacılar segmentinde herhangi bir kayma eksikliği birikimi gözlemlenmedi. Bahsedilen iki segment haricindeki altı segmentin üçü orta, üçü büyük deprem üretme potansiyeline sahiptir. Günümüzde Karlıova, Kaleönü-Beyhan, Palu-Sivrice, Taştepe, Çelikhan-Erkenek, Gölbaşı-Pazarcık segmentleri sırasıyla M 7.0, M 6.9, M 7.1, M 6.8, M 6.9, M 7.4 depremleri üretebilmektedir. Karlıova, Palu-Sivrice, Taştepe ve Gölbaşı-Pazarcık segmentleri ise günümüzde bir önceki döngüde ürettikleri deprem potansiyeline sahiptir. Kayma eksikliği oranları ve b-değerleri arasında, b-değerlerinin kilitli/krip yapan segmentleri ayırt edebilmek için kullanılabileceğini doğrulayan ters bir korelasyon gözlemlendi.

TABLE OF CONTENTS

ACKNOWLEDGEMENTS iii
ABSTRACT iv
ÖZET v
LIST OF FIGURES vii
LIST OF TABLES x
LIST OF SYMBOLS xi
LIST OF ACRONYMS/ABBREVIATIONS xii
1. INTRODUCTION 1
1.1. Anatolian Tectonics 1
1.2. East Anatolian Fault 3
1.3. Historical Earthquakes 7
1.4. Fault and Earthquake Mechanics 10
2. Data Analysis 15
2.1. GPS Data 15
2.2. Back-slip Calculation 16
2.3. Slip Deficit Inversion 18
2.4. Moment Magnitude Forecasting 20
2.5. Frequency-Magnitude Distribution (b-value) 22
3. Results 25
3.1. Slip Deficit Distribution 25
3.2. Current Earthquake Potential 31
4. DISCUSSION 37
4.1. Historical Earthquakes and Segmentation 37
4.2. Slip Deficit Release and Locking Depth 39
4.3. B-value and Slip Deficit Distribution 41
4.4. January 24, 2020 Elazığ Earthquake 42
5. CONCLUSION 44
REFERENCES 46

LIST OF FIGURES

Figure 1.1. The basic tectonic map of Turkey showing major tectonic structures around the Anatolian block (Map was constructed by combining the data from Bozkurt (2001) and Bird (2003).). (Major arrows shows the relative movement of the plates, lines with half arrows show the strike slip fault boundaries, lines with triangles indicate the thrust belts, lines with empty triangles indicate the subduction zones. The bold lines with dashes indicate normal faulting. The dashed line with lines at both sides shows the West Anatolian Extensional Province.). 2

Figure 1.2. Seismicity of the Eastern Turkey. The data is from earthquake catalogue (between M 0.2 and M 7.1) of Kandilli Observatory and Earthquake Research Institute between years 1980 and 2018. Black dots are earthquakes; grey lines are active fault lines from Emre *et al.* (2013); MTJ: Maraş Triple Junction; KJ: Karlıova Junction. . 4

Figure 1.3. Study area, segmentation of the EAFZ and latest ruptures of the segments. The bold black line indicates the segments of the EAFZ. Large white dots indicate the epicentres of the latest major earthquakes of the segments. (Grey lines are active fault lines from Emre *et al.* (2013).) 7

Figure 1.4. Historical earthquakes of the EAFZ over magnitude 6.5 in the last 1000 years. (The earthquakes are shown in Table 1.1., fault map is taken from Emre et al. (2013).). 8

Figure 1.5. Types of faults; (a) normal fault, (b) reverse fault and (c) strike slip fault. 11

Figure 1.6. Stages of earthquake energy build up and release. A. Initial Stage: Before the strain energy builds up and deforms the land. B. Interseismic Stage: When the strain is built up and deforms the land. C. Co-seismic Stage: The sudden release of the strain energy and land returning back to its initial stage. 13

Figure 1.7. Accumulation and release of strain during interseismic and co-seismic stages are shown in graphs. 14

Figure 1.8. Strain rate over time graph, showing the cycle between interseismic, co-seismic and post-seismic stages. 14

Figure 2.1. A typical GPS measurement profile across a fault zone. Grey arrows show tectonic slip rates, which become slower as they approach to the fault. (Right) Back-slip vectors used to quantify inter-seismic accumulation of slip deficit. 17

Figure 2.2. Cross section of a fault plane. 21

Figure 2.3. Frequency-magnitude distribution (FMD) example of the EAF between 1998 and 2018. The data is from earthquake catalogue (between M 0.2 and M 7.1) of Kandilli Observatory and Earthquake Research Institute (KOERI) between years 1980 and 2018. 23

Figure 3.1. GPS measurements compiled from Aktug et al. (2016), Aktug et al. (2013), Alchalbi et al. (2009), Reilinger et al. (2006) and Özdemir *et al.* (2006) CORS (Turkey) stations. Black lines show the active fault line (fault map is taken from Emre et al. (2013). 26

Figure 3.2. Smoothing factor optimization. 26

Figure 3.3. a) Observed and modelled back-slip data are shown with black and red vectors, respectively. Black lines are the active fault lines from Emre et al. (2013). b) Annual slip deficit rate model. 27

Figure 3.4. a) Annual slip deficit rate model. b) b-value model along the fault line. 29

Figure 3.5. Examples of b-value graphics; a) High b-value graphic. b) Low b-value graphic. (The data used in creation of these graphics is from AFAD earthquake catalogue between 2005 and 2019.) 31

Figure 3.6. Accumulated total slip deficit from the latest failure of the segments. 32

Figure 3.7. Current magnitude potentials of the segments are shown. (* Magnitude forecasting confirmed by the January 24, 2020 M 6.8 Earthquake; grey lines are active fault lines from Emre *et al.* (2013).) . 34

Figure 4.1. Temporal variation of magnitude for M 6.5+ earthquakes for the time period of 1000-2000. Also shown in Table 1.1. 37

Figure 4.2. Comparison between seismic and geodetic slip during the last millennia. 40

Figure 4.3. Along fault distribution of January 24th, 2020 Elazığ earthquake and aftershocks. The red dot indicates epicentre of the M 6.8 main shock and blue dots indicate epicentres of the aftershocks (KOERI). Bold black line shows segments of the EAFZ we suggested in this study. Current magnitude potentials and latest rupture dates of the segments are shown. The thin black lines are the active fault lines taken from Emre et al. (2013). 43

LIST OF TABLES

Table 1.1. Historical earthquakes in the last 1000 years on the EAFZ. (Data sources are a is Ambraseys 1989, b is Ambraseys & Jackson, 1998, c is Ambraseys, 2001, d is Grünthal & Wahlström, 2012, and e is KOERI earthquake catalogue. 9

Table 3.1. Segmentation, slip rates and latest failure of segments. (* Magnitude forecasting confirmed by the January 24, 2020 M 6.8 Earthquake.) 35

LIST OF SYMBOLS

a	Constant a (a-value)
b	Constant b (b-value)
A	Area of fault plane
C_r	Covariance matrix of solutions
d	Slip size
M	Magnitude
$\bar{M}$	Average magnitude of the earthquake catalogue
M_{min}	Lowest magnitude of the earthquake catalogue
M_c	Magnitude of completeness
M_0	Seismic Moment
M_w	Moment magnitude
N	Number of earthquakes
n	Number of sites
r	Station position vector
R	Rotation matrix to local coordinate system
t_k	Step size
v_1	Velocity vector
v_2	Velocity vector
x	Vector product operator
$x^{(k)}$	Original point
$x^{(k+1)}$	Point
$\nabla x^{(k)}$	Direction
Ω	Euler rotation vector
σ	Variance factor
μ	Shear modulus

LIST OF ACRONYMS/ABBREVIATIONS

AFAD	Ministry Of Interior Disaster And Emergency Management Presidency
DAF	Doğu Anadolu Fayı
DSF	Dead Sea Fault
EAF	East Anatolian Fault
EAFZ	East Anatolian Fault Zone
FMD	Frequency-Magnitude Distribution
GPS	Global Positioning System
KOERI	Kandilli Observatory and Earthquake Research Institute
Lat	Latitude
Lon	Longitude
LSQ	Least Squares Estimation
M	Magnitude
ma	A million years
Mc	Magnitude of completeness
MLE	Maximum Likelihood Method
MTA	General Directorate of Mineral Research and Exploration
NAF	North Anatolian Fault
NAFZ	North Anatolian Fault Zone

1. INTRODUCTION

1.1. Anatolian Tectonics

Being one of seismically the most active regions, Turkey has been shaken by many constructive earthquakes through the last century. The main reason of these earthquakes is westward movement of the Anatolian plate. This movement has started in the middle Miocene (∼5 ma) with the northward convergent movement of African plate. Arabian and Eurasian plates started to move convergently in the Late Cretaceous (∼90 ma) and the compression in between caused the Anatolian block to move westward (Dewey and Sengor, 1979; Sengor and Yılmaz, 1981; Jackson and McKenzie, 1988; Bozkurt, 2001; Cetin *et al.*, 2003).

These plate movements play a major role in the seismic activity in Anatolia (Cetin *et al.*, 2003). Anatolian plate can be called Anatolian block since it is much smaller and the movement of the block is different than surrounding plates. In the East, the Arabian plate moves with a slip rate of 15 mm/y towards the North forming a thrust belt. The African plate is moving towards northeast with a slip rate of 5 mm/y and developing a strike slip fault, namely Dead Sea Fault (DSF hereafter) as a plate boundary with the Arabian Plate. Northward movement of the African plate generated a subduction zone beneath the Anatolian plate, namely Cyprian and Hellenic Arcs (Bozkurt, 2001; Delph *et al.*, 2015).

As shown in Figure 1.1 the major empty arrows show relative movement of the Anatolian block with respect to the stable Eurasian plate, which occurs with a rate of 21 mm/y and westward in the East, with a rate of 33 mm/y towards southwest near the Hellenic Arc in the West, representing a counter-clockwise movement with respect to an Euler pole near Alexandria (Bozkurt, 2001; Delph *et al.*, 2015). This movement generates an extensional region in the western Anatolia, which is one of the fastest extending and seismically active region in the Earth according to Bozkurt

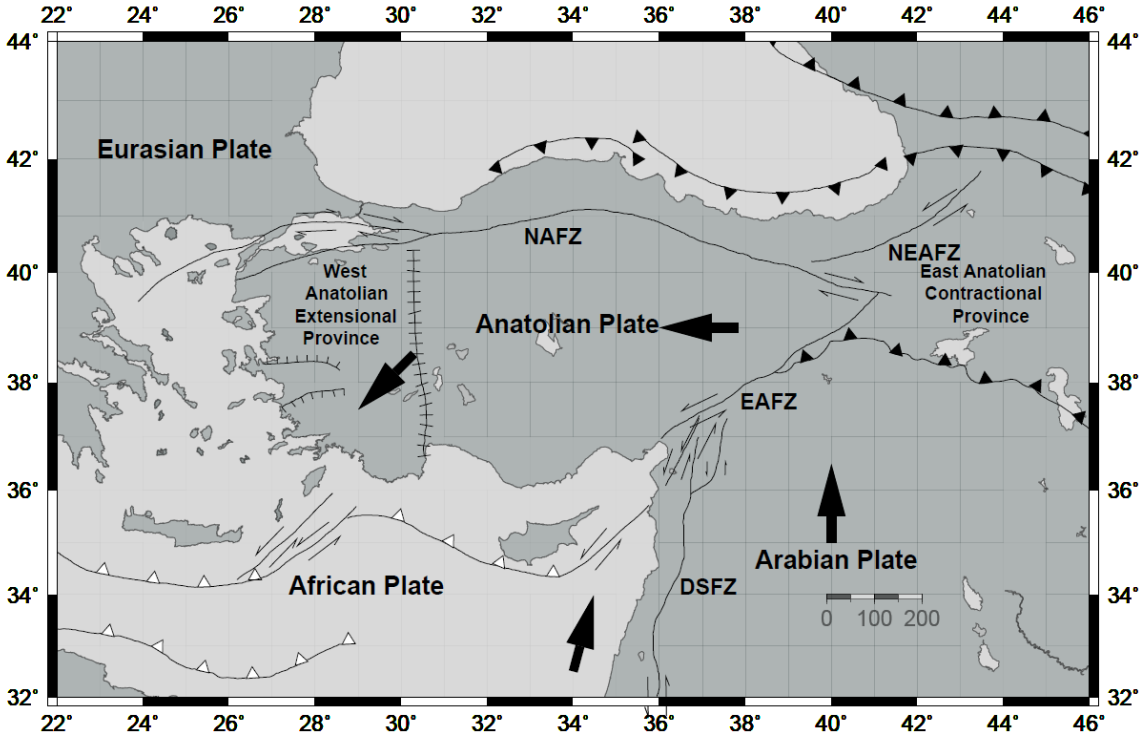

Figure 1.1: The basic tectonic map of Turkey showing major tectonic structures around the Anatolian block (Map was constructed by combining the data from Bozkurt (2001) and Bird (2003).). (Major arrows shows the relative movement of the plates, lines with half arrows show the strike slip fault boundaries, lines with triangles indicate the thrust belts, lines with empty triangles indicate the subduction zones. The bold lines with dashes indicate normal faulting. The dashed line with lines at both sides shows the West Anatolian Extensional Province.).

(2001). Unlike in the extension in the west, in the East Anatolia Region accommodates a compressional tectonic regime developed between Arabian and Eurasian plates.

The westward movement of Anatolian block occurs at a slip rate of 20-25 mm/y (Reilinger *et al.*, 1997; McClusky *et al.*, 2000; Nalbant *et al.*, 2002; Cetin *et al.*, 2003). There are two major faults representing the boundaries of the Anatolian block, that namely the North Anatolian Fault (NAF hereafter) and the East Anatolian Fault (EAF hereafter). In the north of Anatolian block, the NAF accommodates a dextral movement at a slip rate of 25 mm/y. In the south, however, the EAF accommodates a sinistral movement at a slip rate of 10 mm/y. The NAF extends for 1250 km from Karlıova junction in the east to the Aegean Sea in the west (Sengor, 1979). The EAFZ extends for more than 500 km from the Karlıova junction, where it conjugates the NAFZ, and to Maraş triple junction, where the fault joins the DSF and the Cyprian Arc (Çetin *et al.*, 2003; Bulut *et al.*, 2012). In the last century, the NAF is seismically more active than the EAF (Ambraseys, 1971).

1.2. East Anatolian Fault

The EAF is the second most active fault in Turkey, that operates in south-east passing through several cities; Bingöl, Elazığ, Malatya, Adıyaman and Kahramanmaraş. The earthquake activity of Eastern Turkey from the earthquake catalogue (between M 0.2 and M 7.1) of Kandilli Observatory and Earthquake Research Institute (KOERI hereafter) between years 1980 to 2018 is shown in Figure 1.2. The EAF operated with a slip rate of 10 mm/y between the Karlıova junction and the Maraş triple junction. Beyond the Maraş junction in the southwest, has a slip rates ranging between 0.7 and 4.5 mm/y (Aktug *et al.*, 2016). In the last century the EAFZ did not generate any large earthquake but historical earthquakes documents that it generated large earthquakes in the past (e.g. November 29, 1114 M 7.8, March 28, 1513 M 7.4, and March 2, 1893 M 7.1), and have the potential to generate large earthquakes in future (Ambraseys, 1989; Ambraseys & Jackson, 1998).

The EAF has started to develop in late Pliocene (2-3 Ma) according to Şaroğlu *et al.* (1992), Westaway and Arger (2001). The fault system was firstly mentioned by Allen (1969). Its left lateral strike slip character and possible connection to the DSF was firstly discovered by Arpat & Şaroğlu (1972).

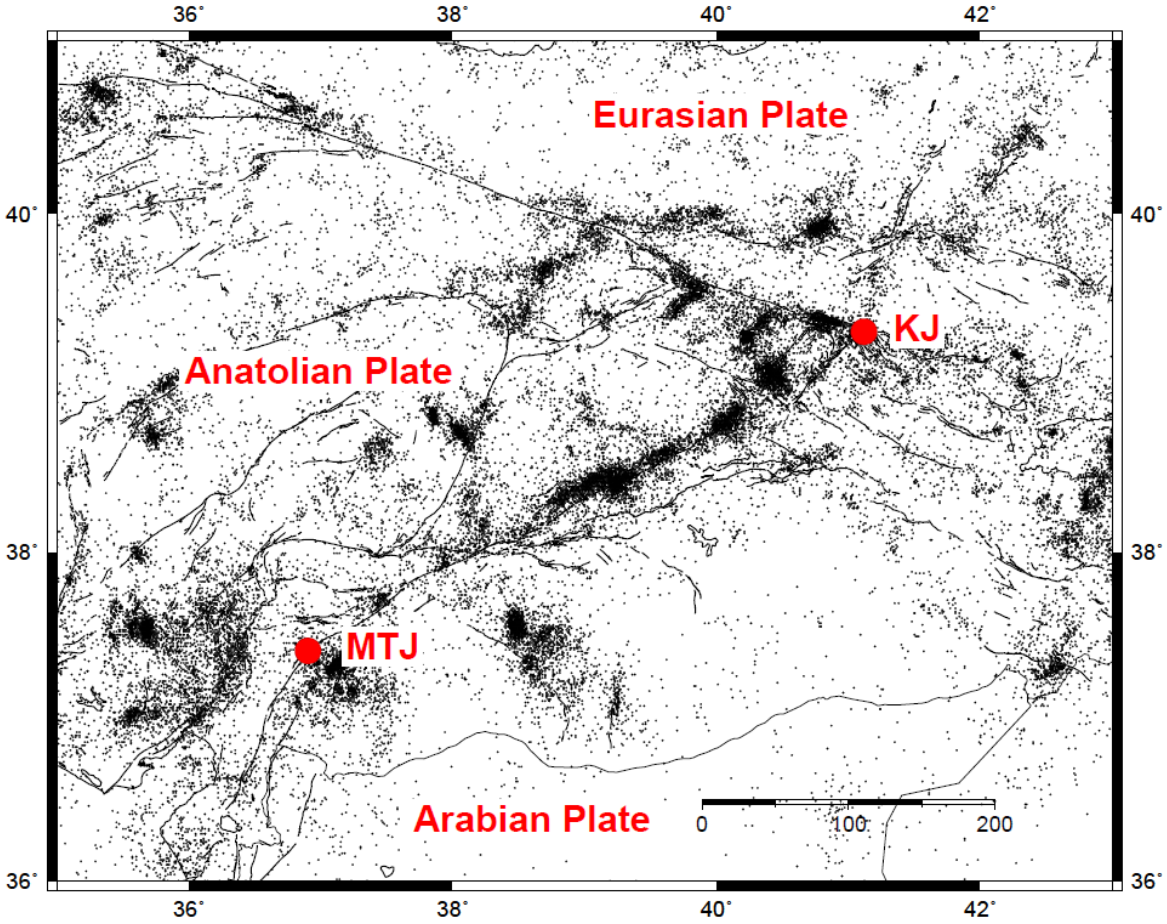

Figure 1.2: Seismicity of the Eastern Turkey. The data is from earthquake catalogue (between M 0.2 and M 7.1) of Kandilli Observatory and Earthquake Research Institute between years 1980 and 2018. Black dots are earthquakes; grey lines are active fault lines from Emre *et al.* (2013); MTJ: Maraş Triple Junction; KJ: Karlıova Junction.

There are several studies that describe the structure of the EAF and its segmentation. The studies investigated segmentation according to segment trends and geometries, their discontinuities and step overs, the surface ruptures and earthquakes

they accommodated. Arpat & Şaroğlu (1972) only mentioned eastern segments between Karlıova and Hazar Lake. A later study by Şaroğlu *et al.* (1992) divided the EAF between Karlıova and Antakya to six segments while the same section has divided to eleven segments by Herece (2008). Hempton *et al.* (1981) mentions five segments. Barka & Kadinsky-Cade (1988) mentions fourteen segments. Finally, a recent study by Duman & Emre (2013) suggests that there are seven segments on the main strand, and nine segments on the Northern strand. The EAF has segments with high and low frictional strengths. Low frictional strength might accommodate steady sliding while the high frictional segments can accumulate large slip deficit and therefore generate strong/major earthquakes (Duman & Emre, 2013; Aktuğ *et al.*, 2016).

In this study, the fault zone is divided into eight segments based on historical earthquake, available fault maps reviewing all previous studies. The segmentation that we adopt is described below in a northeast to southwest order. It is also shown in Figure 1.3.

(1) The northernmost segment is the Karlıova, starting from the Karlıova junction between the NAFZ and the EAFZ (Duman & Emre, 2013). The stress evolution of the EAFZ study by Nalbant *et al.*, in 2002 and MTA (1992) fault rupture data defines this segment. The segment is 35 km long.

(2) Karlıova segment is followed by Hacılar segment, which starts at Göynük district and extends to Göltepesi region. The segment was defined by the ruptures from historical earthquakes (MTA, 1992; Nalbant et al, 2002) as well as the segmentation study by Emre *et al.*, 2010 and Duman & Emre, 2013. This segment has a length of ∼23 km.

(3) The next segment is Kaleönü-Beyhan, starts from Kaleönü region and extends towards Palu. Its length is ∼73 km. The segment is defined as a restraining bend and being the largest jog structure, where 17 degrees' change is observed of the strike of the EAF by Duman & Emre (2013).

(4) Palu-Sivrice segment extends from Palu to western tip of the Hazar lake near Sivrice for ∼64 km length. Palu-Sivrice segment was defined by the combined data from MTA rupture map (1992), AFAD earthquake catalogue and study of Nalbant *et al.* (2002) and Duman Emre (2013).

(5) The next segment to the further southwest is 55 km long Sivrice-Pütürge segment that starts from western tip of The Hazar Lake and extends towards Pütürge region. Previously ruptured on March 27, 1875 (M 6.8) (MTA Rupture Map, 1992; AFAD; Ambraseys, 1988) and aftershocks of Elazığ earthquake (M 6.8) (2020) hypocentre locations from AFAD also support the segmentation.

(6) Taştepe segment extends between Pütürge and Sincik regions. Its length is 23 km. The segment is defined by the rupture of the latest major earthquake on December 4, 1905 (M 6.8) (Ambraseys & Jackson, 1998). MTA (1992) rupture map and stress evolution map of Nalbant *et al.* (2002) verifies its segment boundaries.

(7) Çelikhan-Erkenek segment is between the Çelikhan and Erkenek regions. Its length is 47 km. This segment is defined by the Nalbant *et al.* (2002) stress evolution map and MTA historical earthquake rupture map (1992).

(8) Gölbaşı-Pazarcık segment is the last segment and it is between the Yaylacık and Kocalar regions and its length is 92 km. Segment boundaries are supported by Nalbant *et al.* (2002) and fault map by MTA (1992).

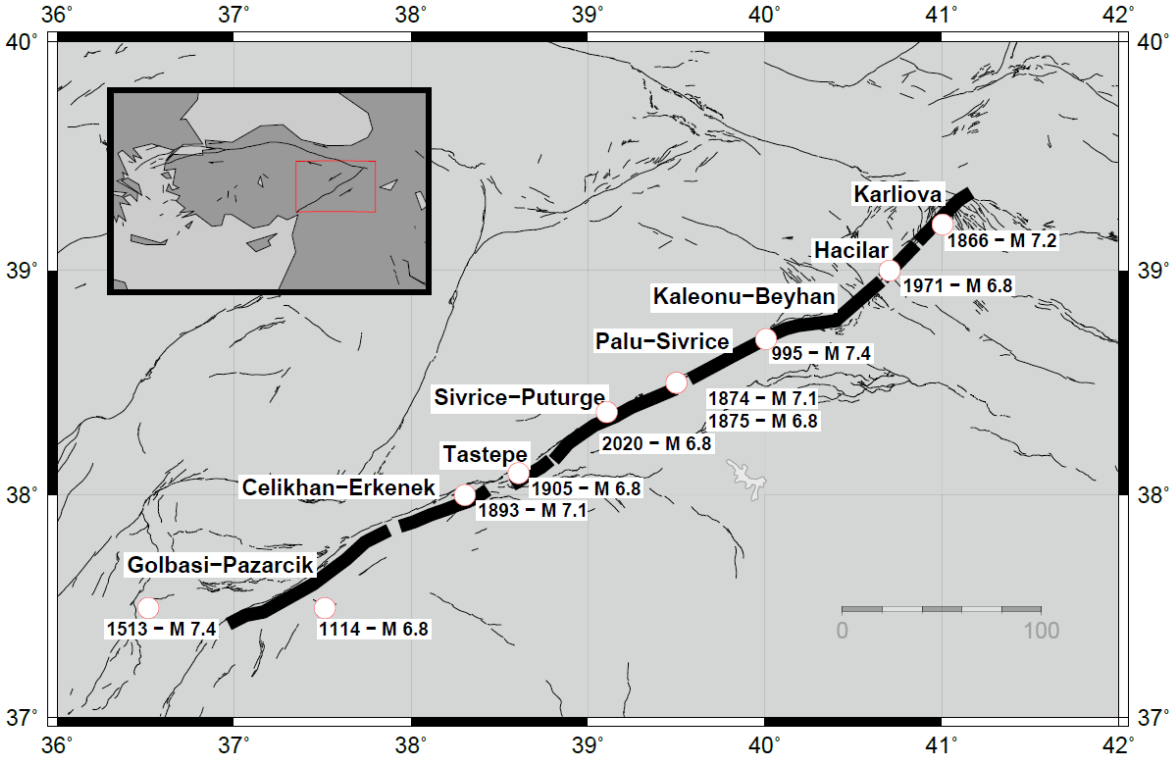

Figure 1.3: Study area, segmentation of the EAFZ and latest ruptures of the segments. The bold black line indicates the segments of the EAFZ. Large white dots indicate the epicentres of the latest major earthquakes of the segments. (Grey lines are active fault lines from Emre *et al.* (2013).)

1.3. Historical Earthquakes

Historical earthquakes are important to understand the structure of and activity of the fault zone. The EAFZ has generated many large earthquakes within the last millennium. Historical earthquakes of the EAFZ within the last 1000 years are shown in Figure 1.4 and listed in Table 1.1.

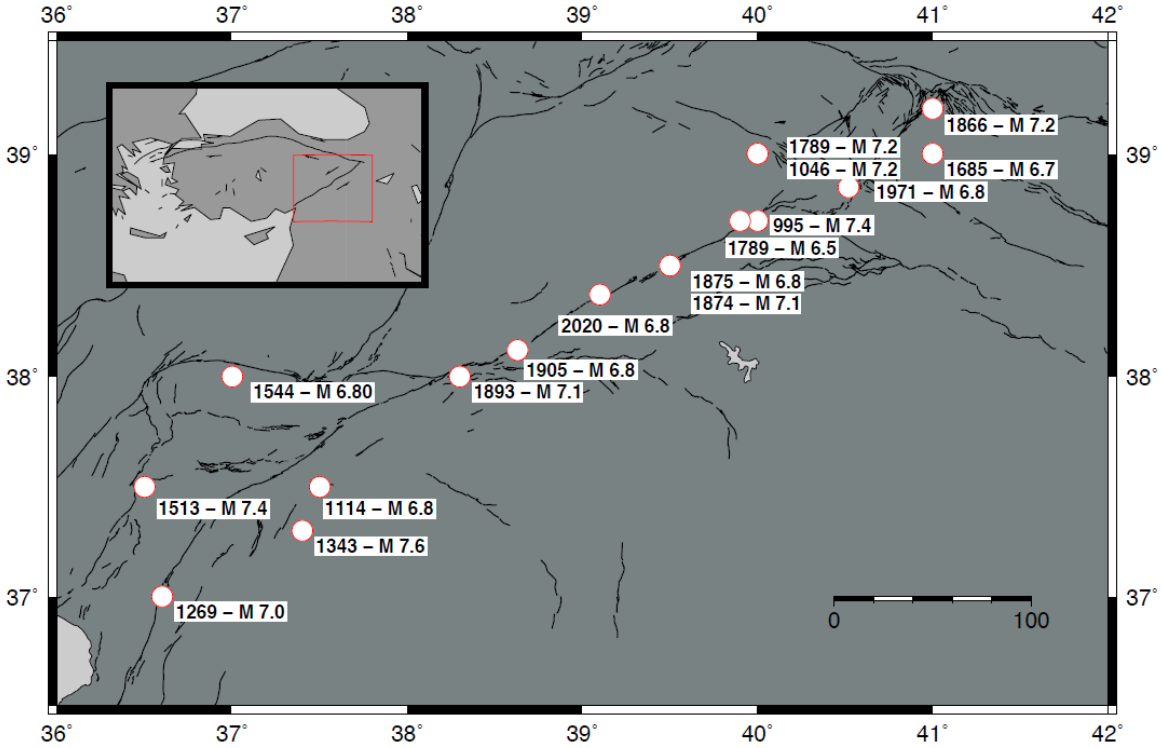

Figure 1.4: Historical earthquakes of the EAFZ over magnitude 6.5 in the last 1000 years. (The earthquakes are shown in Table 1.1., fault map is taken from Emre et al. (2013).).

Historical earthquake data indicate that there were specific time periods where the EAF was seismically more active than the NAF, and vice versa (Ambraseys, 1971). The largest three earthquakes reported in the last 1000 years are November 29, 1114 (M>.8), March 28, 1513 (M>7.4) and March 2, 1893 (M>7.1) (Ambraseys & Jackson, 1998). During the last century, there were only two M>6.5 earthquakes along the EAFZ (December 4, 1905, M 6.8 and May 22, 1971 M 6.8) (Ambraseys & Jackson, 1998). Although the EAFZ did not generate any large earthquakes (M>7) in the last century, historical earthquakes document that the EAFZ has potential to generate large earthquakes. The current quiescence of the fault zone is interpreted to represent that the fault is locked (Bulut *et al.*, 2012).

Table 1.1: Historical earthquakes in the last 1000 years on the EAFZ. (Data sources are a is Ambraseys 1989, b is Ambraseys & Jackson, 1998, c is Ambraseys, 2001, d is Grünthal & Wahlström, 2012, and e is KOERI earthquake catalogue.

Date	Magnitude	Latitude	Longitude	Source
- / - /995	7.4	38.7	40	b, d
29/11/1114	6.8	37.5	37.5	b, d
18/12/1121	7	38.5	37.8	d
17/04/1269	7	37	36.6	d
- / - /1343	7.6	37.3	37.4	d
28/03/1513	7.4	37.5	36.5	a, d
22/01/1544	6.8	38	37	a, b, d
22/11/1685	6.7	39	41	d
29/05/1789	7.1	39	40	a
- / - /1789	6.5	38.7	39.9	d
12/05/1866	7.2	39.2	41	b
20/06/1866	6.8	38.5	40.9	a, d
03/05/1874	7.1	38.5	39.5	a, b
27/03/1875	6.7	38.5	39.5	b
02/03/1893	7.1	38	38.3	a, d
31/03/1893	7	38.4	38.7	b, d
04/12/1905	6.8	38.1	38.6	b
22/05/1971	6.8	38.8	40.5	c
08/03/2010	6	38.7	40.1	e
24/01/2020	6.8	38.37	39.1	e

There are segments that have not had an earthquake over thousand years. The last destructive earthquake happened in January 24, 2020, namely Elazığ earthquake (M 6.8), which re-ruptured the segment that were ruptured during the March 27, 1875 (M 6.8) earthquake. Based on this reactivation period of this segment might be 145 years although it needs to be verified by more earthquakes in the past. This is an example on how historical earthquakes can help understand the reactivation periods of the fault segments.

1.4. Fault and Earthquake Mechanics

To understand the mechanics of earthquakes and faults, we should first understand the tectonic plates and their movement as a driving force of these catastrophic events and structures. Earth crust is subdivided into many blocks with discontinuous margins, which are called tectonic plates and faults, respectively. The thickness of the crust range from 8.0 to 45.0 km depending on its age and tectonic role, e.g., oceanic crust is thin as its age is relatively young and is not exposed to tectonic collision while continental crust is thick as its age is relatively old and exposed to dense tectonic deformations at plate boundaries. These plates move under the force generated mainly by the convectional movement of magma in the mantle, gravitational pull along subduction zones and gravitational push along oceanic ridges (Cox & Hart, 1986; Davies & Richards, 1992, Lutgens & Tarbuck, 2016).

The plates move mainly in three types; convergent, divergent and transform. Convergent movement is when two plates move towards each other. This movement can generate two types of boundaries, namely continental collision zone or subduction zone (Lutgens & Tarbuck, 2016). Continental collision zone can occur on continental crust where two plates collide. This boundary thickens the continental crust and form the mountains (Royden, 1993). Subduction zones occur on oceanic crust when one of the converging plates goes under the other plate due to density contrast between the plates (Stern, 2002).

Divergent boundaries occur where two plates diverge from each other with respect to the boundary in between. This type of movement generates new oceanic crust along the oceanic ridges. The third type of boundary is transform boundaries where two plates move sub parallel to each other in opposite directions along the boundary in between (Lutgens & Tarbuck, 2016).

These boundaries accommodate different type of faults although they have their own single overall tectonic regimes. There are mainly three types of faults, namely normal, reverse (thrust) and strike slip faults as shown in Figure 1.5. Normal faults occur by crust pull apart. Hanging wall moves down relative to the foot wall. Reverse fault occurs when crust is under compression. In this case the hanging wall moves upward relative to foot wall. When crust moves past each other. If one side moves to the left relative to the other one, it is called sinistral (left-lateral strike slip) fault. If it moves to the right relative to the other one, it is called dextral (right-lateral strike slip) fault. The two major plate boundaries in Turkey, namely the EAF and the NAF exemplify a sinistral and a dextral fault, respectively (Lutgens & Tarbuck, 2016).

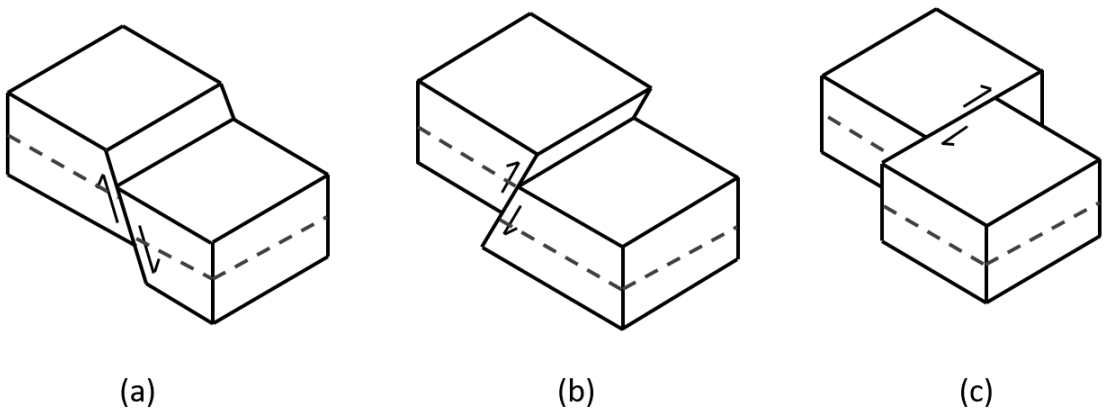

Figure 1.5: Types of faults; (a) normal fault, (b) reverse fault and (c) strike slip fault.

Earthquake happens when the stored strain energy over tens/hundreds of years releases suddenly in a few seconds. Elastic rebound theory is how energy is stored and released during an earthquake (Reid, 1910). In response to tectonic loading, sides of

the faults are locked where the frictional strength is high, or slides where the frictional strength is low along the fault plane.

Strain energy starts being accumulated as observed as an elastic deformation at the surface. The initial stage is before the strain is built up and deform the land. This stage is called interseismic stage. Interseismic stage can continue for a long time. The stage finishes when the built up strain energy exceeds the strength of the fault. This can be the frictional strength of the fault or the asperity that is locking the fault.

When the stored energy exceeds the strength of the fault, fault slides abruptly and generates an earthquake, as observed as a plastic deformation at the surface. This sudden release stage is called co-seismic stage. Co-seismic stage occurs in seconds. After the co-seismic stage there is the post-seismic stage. This stage can last days, months even years after the earthquake (Scholz, 2002). Following the earthquake, the energy distribution gets back to the initial stage as shown in Figure 1.6. During interseismic stage strain accumulation is shown with Δx in Figure 1.7. The co-seismic release can also be a maximum of Δx, if the fault plane is homogenous and all the strain releases at once. Figure 1.8 shows the cycle of interseismic, co-seismic and post-seismic stages.

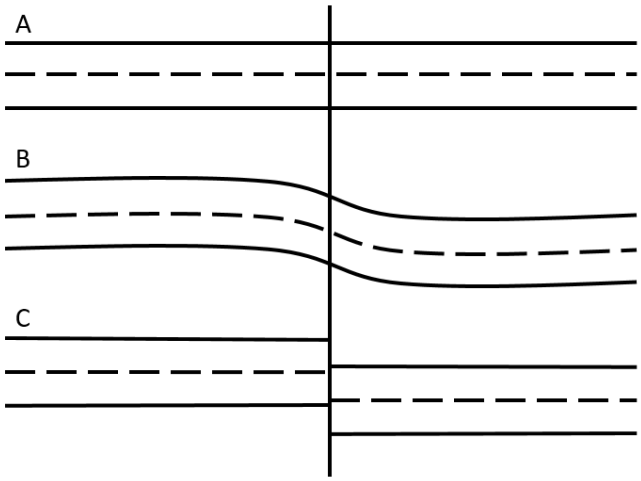

Figure 1.6: Stages of earthquake energy build up and release. A. Initial Stage: Before the strain energy builds up and deforms the land. B. Interseismic Stage: When the strain is built up and deforms the land. C. Co-seismic Stage: The sudden release of the strain energy and land returning back to its initial stage.

The origination point of an earthquake under the surface is called hypocentre while its surface projection is called epicentre. There are relatively small size earthquakes preceding the main one, which are called foreshocks. The largest earthquake in an earthquake sequence is called main-shock. The smaller earthquakes occurring after the main-shock are called aftershocks. Aftershocks are observed during the post-seismic stage (Lutgens & Tarbuck, 2016).

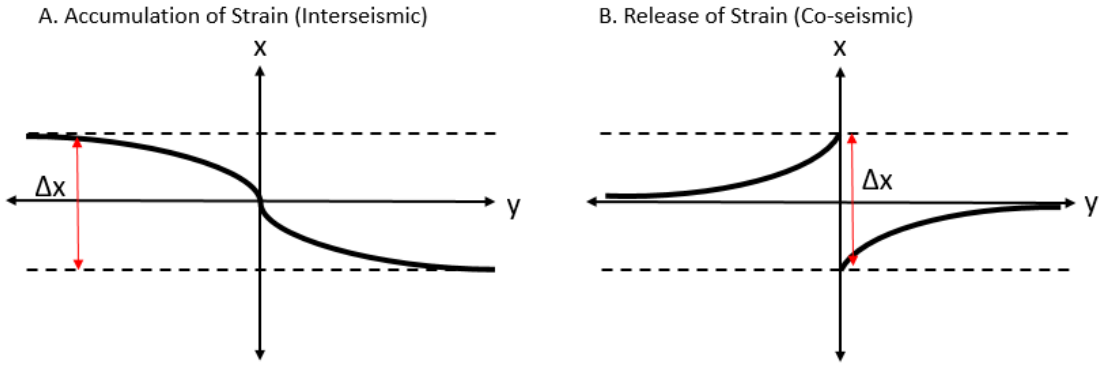

Figure 1.7: Accumulation and release of strain during interseismic and co-seismic stages are shown in graphs.

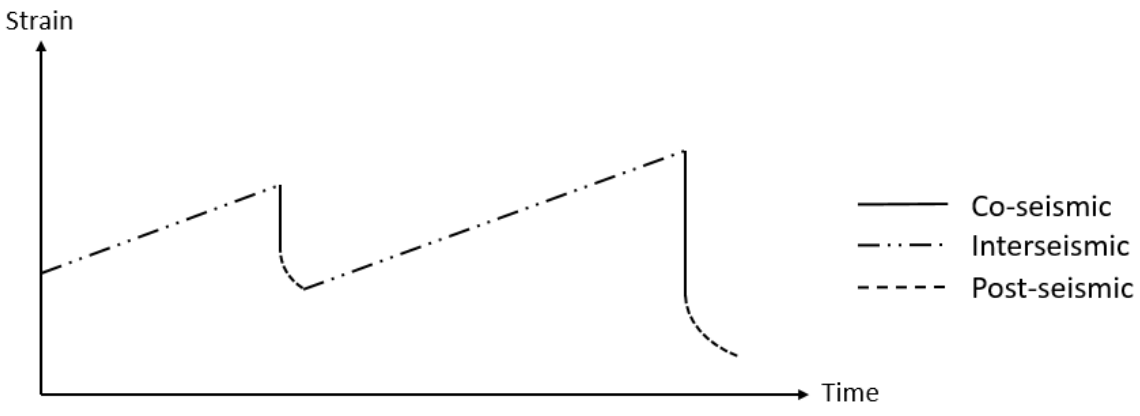

Figure 1.8: Strain rate over time graph, showing the cycle between interseismic, co-seismic and post-seismic stages.

2. Data Analysis

The primary objective of this study is to characterize the deformation along the EAFZ and to forecast size of future earthquakes based on the time window the segments store the deformation. This requires three basic input, amount of deformation, segmentation and the historical earthquakes along the fault zone.

The time predictable recurrence model for large earthquakes by Shimazaki & Nakata (1980) mentions that slip of the next large earthquake is equal to the slip deficit accumulated since the last earthquake. For the calculation of the slip deficit, back-slip data obtained from surface velocities can be used (Savage, 1983). After calculating the back-slip data, it needs to go under slip deficit inversion process. This process will project the slip deficit onto the fault plane, where the rupture potentially will be. Slip deficit then can be used to calculate moment magnitude based on segment sizes. Through these processes, the magnitude of a possible earthquake can be quantified.

2.1. GPS Data

First of all, we need the slip rate along the fault zone. This can be achieved by GPS measurements. Our strategy is to collect GPS measurements from previous studies. The collected data should be transformed to the same reference system to minimize artificial variations. Euler matrix rotation is used to unify the data to avoid errors that can be generated by different reference systems used in different studies (Aktuğ *et al.*, 2009; Bulut *et al.*, 2019). In this study, we used data compiled by Aktug *et al.* (2016), from the measurements of Aktug *et al.* (2016), Aktug *et al.* (2013), Alchalbi *et al.* (2009), Reilinger *et al.* (2006) and Özdemir *et al.* (2006) CORS (Turkey) stations. The compiled GPS data are transformed to the reference frame of Reilinger *et al.* (2006), because it has the highest common stations (Aktuğ *et al.*, 2009, 2013, 2016). Transformation combination is given below.

$$v_2 = v_1 + R\,(\Omega\ x\ r) \tag{2.1}$$

where v_1 and v_2 are velocity vectors in each frame, R is the rotation matrix to local coordinate system from Cartesian system, Ω is vector of Euler rotation, x is vector product operator and r is the position vector of each station (Aktuğ *et al.*, 2009, 2013, 2016; Bulut *et al.*, 2019).

$$\sigma_0^2 = \frac{r^T c_r^{-1} r}{2n-3} \tag{2.2}$$

The second equation is how the reference variance factor is obtained. There r is the residual vector between the GPS velocities and their difference from the average, C_r is the covariance matrix of solutions of , and n is the number of sites (Aktuğ *et al.*, 2009; Nocquet, 2012).

2.2. Back-slip Calculation

Based on elastic rebound theory, before the sudden release of energy and generation of an earthquake the strain, and therefore slip deficit, must be accumulated to exceed the frictional strength along the ruptured fault segment (Reid, 1910). The back-slip can be used to observe slip deficit during the interseismic stage, the stage between the two successive failures of the same segment. Near the locked fault plane (near-field), slip rate is lower than rate of the plate movement (far-field). This shows the strain in the vicinity of the fault due to on-fault friction and can be observed by GPS measurements at surface.

We use the GPS data compiled from different measurements to calculate the back-slip vectors. As illustrated in Figure 2.1, we subtract far-field velocity from all the velocities to obtain back-slip data, which is predominant in the near field.

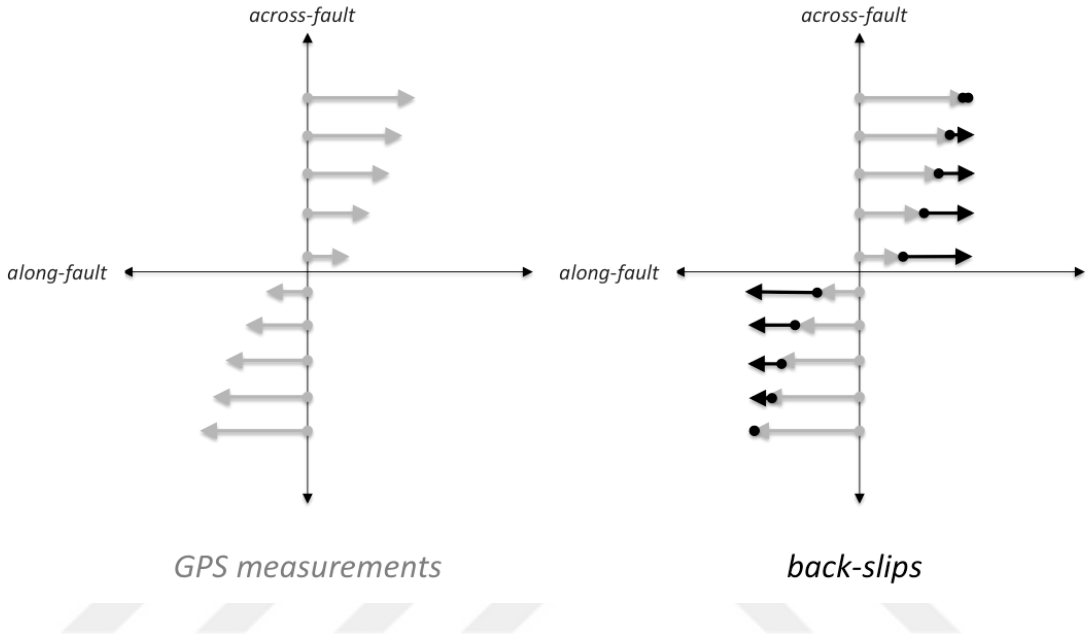

Figure 2.1: A typical GPS measurement profile across a fault zone. Grey arrows show tectonic slip rates, which become slower as they approach to the fault. (Right) Back-slip vectors used to quantify inter-seismic accumulation of slip deficit.

The next step is choosing the far-field velocity. Far-field velocity is chosen taking the farthest possible velocity vector from the fault line. The reason for this is that the farthest the vector is the least affected by the friction on the fault. The average of the far-field vectors is taken, when there are multiple velocity vectors representing the far-field velocity. For obtaining the back-slip, we take the difference between near-field velocities, which are affected by the fault friction, and far-field velocity, which are almost independent of the fault friction.

2.3. Slip Deficit Inversion

The examination of interseismic slip deficit requires a slip deficit inversion. We applied "Steepest descent/gradient" inversion method, which employs Okada's semi-infinite space model simulating elastic Green's functions. By using this method, we can project the annual back-slip measurements onto fault plane as annual slip deficit (Okada, 1985; Wang *et al.*, 2009; Bulut *et al.* 2019).

Formulation of steepest descent method is below:

$$x^{(k+1)} = x^{(k)} - t_k \nabla f\left(x^{(k)}\right) \tag{2.3}$$

Where $x^{(k+1)}$ is a point, t_k is a step size towards direction $\nabla x^{(k)}$, from the original point $x^{(k)}$. The formulation comes from the step by step approach as described in below formulas.

$$x^{(k+1)} = x^{(k)} - t_k \nabla x^{(k)} \tag{2.4}$$

The Equation (2.4) is a formulation of movement, where $\nabla x^{(k)}$ is the steepest direction we move with each iteration. Through this process algorithm is going to find the minimum value of the function for the point. Simply want to find $f(x + d)$, where x is a point and d is movement direction. Through using Taylor expansion Equation (2.5), we can find the steepest direction. The direction d, which find the minimum function has an optimization problem Equation (2.6), as shown in below.

$$f(x+d) \approx f(x) + \nabla f(x)^T d \tag{2.5}$$

$$\min_{\boldsymbol{d}:\|\boldsymbol{v}\|=1} \nabla f(\boldsymbol{x})^T d \tag{2.6}$$

Cauchy-Schwarz inequality indicates that, $\nabla f(x)^T d < \|\nabla f(x)\|\|d\|$; $d = \lambda \nabla f(x), \lambda \in \mathbb{R}$. If $||d|| = 1$;

$$d = \frac{\nabla f(x)}{\|\nabla f(x)\|} \tag{2.7}$$

For obtaining the minimum function, we need the minimum d from $\nabla f(x)^T d$. It can be interpreted as $-d$. We acquire the Equation (2.3) (Kelley, 1962; Tsang *et al.*, 2004).

This inversion method also solves another problem caused by the number of slip deficit blocks. There is a non-uniqueness in slip inversion which is caused by number of slip deficit blocks being significantly greater than the number of GPS measurements. The method fixes this problem by making use of the correlation of strain accumulation and slip deficit as a priori information (Wang *et al.*, 2006).

2.4. Moment Magnitude Forecasting

Moment magnitude simultaneously quantifies the energy and rupture size of an earthquake. Moment magnitude scale was firstly described Hanks & Kanamori (1979). The moment magnitude can be shown with Mw (Hanks & Kanamori, 1979). M can also be used to indicate the magnitude. This scale, unlike the other empirical magnitude scales, can physically, and therefore correctly, quantify magnitude of large earthquakes.

The scale uses seismic moment (M_0) as a base. Seismic moment can be calculated from the area of the fault rupture and the slip of the earthquake based on an assumed shear modulus. Seismic moment calculation is described as follows:

$$M_0 = \mu \cdot A \cdot d \tag{2.8}$$

μ is the shear modulus, which is assumed to be 32 GPa in the Earth's crust. A is the area of the ruptured fault plane. A is calculated multiplying the depth multiplied by the length of the rupture plane. d is the slip created by the earthquake in meters. The description is also shown in Figure 2.2.

Moment magnitude calculation (Hanks & Boore, 1984) is shown in below:

$$M_w = \frac{2}{3} \log (M_0) - 10.7 \tag{2.9}$$

Magnitude forecasting is calculating the magnitude potential of a fault/fault seg-

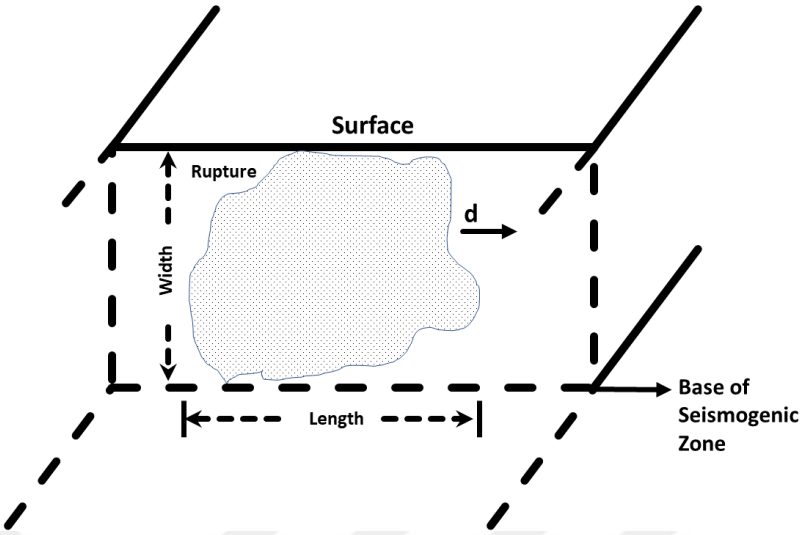

Figure 2.2: Cross section of a fault plane.

ment through the tectonic processes described in section above. Earthquake potential of a fault zone cannot be forecasted entirely since the fault zone does not have a homogenous geometry. Earthquake potential of a fault zone must be rather studied segment by segment. Segment lengths and their seismogenic depths are used to forecast rupture planes of future earthquakes (A in Equation (2.8)).

The segmentation is important for calculating the rupture area and determining the slip deficit. Since all segments might have a different slip deficit, investigating the segmentation is crucial to give more accurate results for magnitude forecasting.

Another factor in the magnitude forecasting is the last major earthquake generated by the fault segment. The last major earthquake date will give us the information of how long the segment has been accumulating strain energy, in other words, the slip deficit. Total slip deficit (d in Equation (2.8)) is calculated from the annual slip deficit rate multiplied by the time passed since the last major earthquake.

2.5. Frequency-Magnitude Distribution (b-value)

Gutenberg & Richter (1956) introduced the relationship between number and magnitude of earthquakes. The relationship describes frequency and magnitude of earthquakes in a specific region and time period. The formula is as given below:

$$\log_{10} N = a - bM \tag{2.10}$$

M is a determined magnitude scale. N is the number of earthquakes, which have equal or greater magnitudes than the determined magnitude M. a and b are constants. M, a and b can vary from region to region. Parameter a defines the seismicity level of a specific region (Okal & Romanowicz, 1994). Higher value of parameter a indicates a high seismicity in the region.

Parameter b or b-value, changes according to the seismic activity in the region. Due to the logarithmic structure of the Equation (2.10), with decreasing magnitude, the earthquake number will increase in multiples of 10. The slope of magnitude versus cumulative number of earthquakes is the b-value as shown in Figure 2.3. To obtain a more accurate b-value, there should be a threshold for the earthquake magnitudes and number of earthquakes in a patch/volume for calculation. Insufficient number of earthquakes will lead to unstable and therefore artificial results.

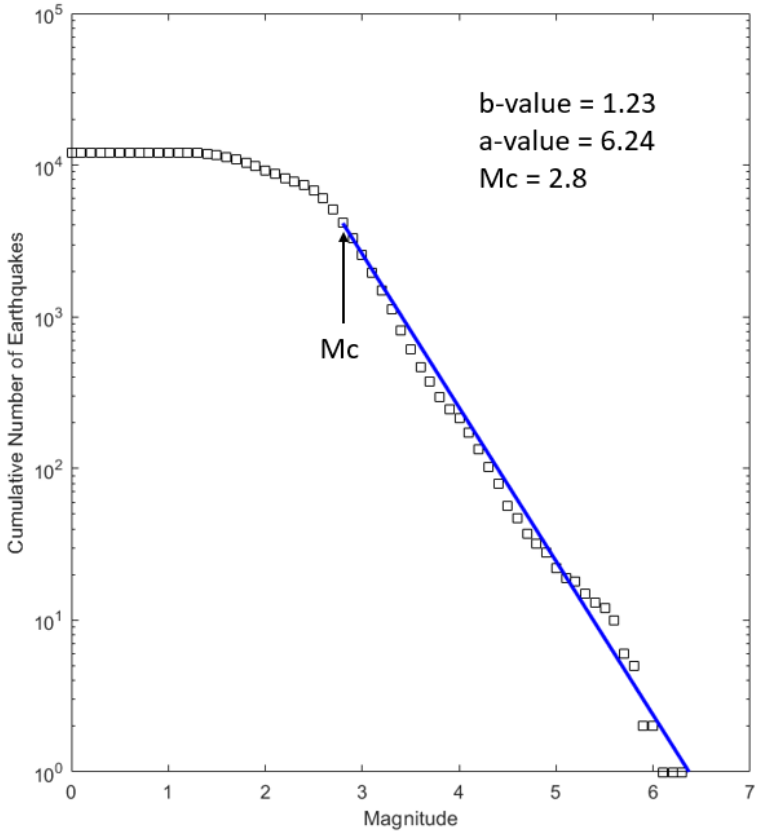

Figure 2.3: Frequency-magnitude distribution (FMD) example of the EAF between 1998 and 2018. The data is from earthquake catalogue (between M 0.2 and M 7.1) of Kandilli Observatory and Earthquake Research Institute (KOERI) between years 1980 and 2018.

This threshold for earthquake magnitudes is called the magnitude of completeness (Mc). It is the minimum magnitude determining the completeness of the earthquake catalogue, in other words, above which all earthquakes are recorded (Mignan & Woessner, 2012). If the Mc is not determined accurately the data will lead to erroneous results. If it is a high value, it can result in a data loss and if it is a lower value, it can result in using an inaccurate data that might artificially affect the results (Mignan & Woessner, 2012). In Figure 2.3 the Mc is 2.8.

There are two ways in order to calculate the b-value. One of them is the least squares estimation (LSQ) and the other one is maximum likelihood estimation (MLE) method. LSQ method is explained by below equation:

$$b = \frac{\sum_{i=1}^{n} \left(X_i - \bar{X}\right)\left(Y_i - \bar{Y}\right)}{\sum_{i=1}^{n} \left(X_i - \bar{X}\right)^2} \tag{2.11}$$

LSQ is used to find the slope of best fitting line between the number of earthquakes in logarithmic base on Y axis and magnitudes on X axis in order to obtain the b-value. Using LSQ might not give an accurate b-value, since LSQ can also use the data smaller than the Mc. LSQ is altered by large earthquakes and effected by outlier data. The equation of second method, MLE is given below (Aki, 1965):

$$b = \frac{\log_{10} e}{\left(\bar{M} - M_{min}\right)} \tag{2.12}$$

Where $\bar{M}$ is the average magnitude, $M_{\min}$ is the lowest magnitude of the earthquake catalogue. We used MLE method in order to obtain b-value. Unlike the LSQ method, MLE is not altered by large earthquakes. It rather threats each earthquake equally.

b-value is used to discriminate creeping or locked faults segments. According to Wyss *et al.* (2004), b-values between 0.5 and 0.7 indicate locked faults, while values between 1.1 and 1.6 indicate creeping faults. In this study, we compared b-value with slip deficit to investigate if there is a spatial correlation and therefore to better constrain creeping and locked fault segments along the EAFZ.

3. Results

3.1. Slip Deficit Distribution

We used the velocity field that has been combined by Aktug *et al.* (2016), from Aktug *et al.* (2013), Alchalbi *et al.* (2009), Reilinger *et al.* (2006) and Özdemir *et al.* (2006) CORS (Turkey) stations and their new GPS measurements. This unified combination has increased also the accuracy of the slip rates as it has eliminated errors due to different reference frames. The distribution of the velocity fields from the studies are shown in Figure 3.1.

Using the unified GPS data, we obtain the back-slip vectors as explained in the section 2.2. Back-slip vectors are high where the strain energy accumulates more and vice versa. Using the back-slip vectors, slip deficit for each segment can be determined along the fault. Using slip deficit inversion method based on back-slip data, back-slip vectors are projected on the fault plane to calculate slip deficit rates. From the last major earthquake occurred on the segment, how much slip deficit accumulated can be determined.

In Figure 3.3a the back-slip vector distribution along the fault line is shown. After the slip deficit inversion, we can demonstrate the annual slip deficit rate on the fault plane, as shown in Figure 3.3b.

In order to demonstrate the effect of smoothing factor on the resulting errors and finding the best data-model correlation, we made a comparison between smoothing factors in Figure 3.2. As shown in Figure 3.2, we determined the finest approximation was achieved by using the 0.05 smoothing factor. The smoothing factor gives a data-model correlation value of 0.9550. We assume that all slip deficits occur on the main fault and deformation on the secondary faults are ignored.

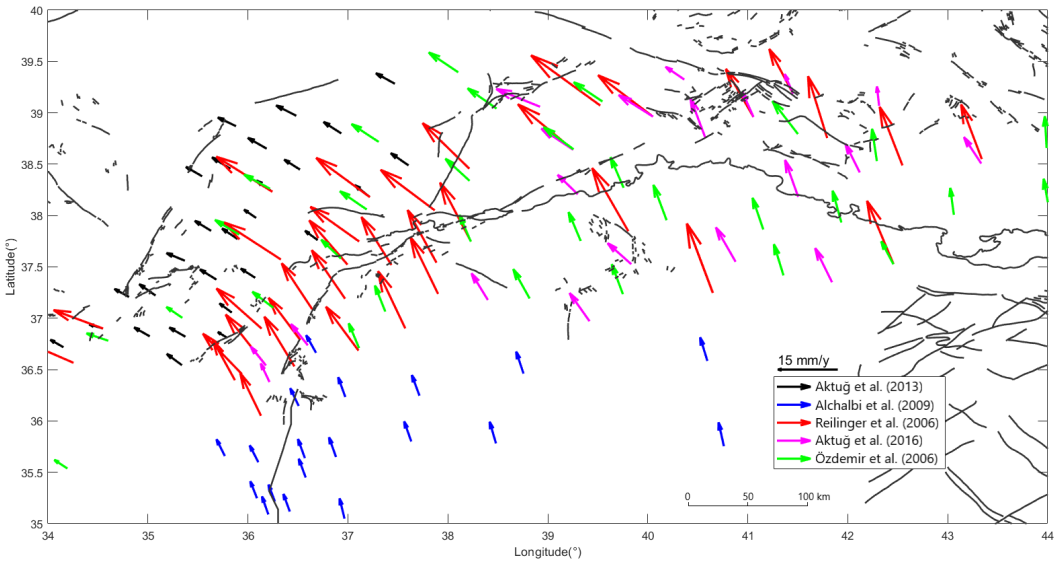

Figure 3.1: GPS measurements compiled from Aktug et al. (2016), Aktug et al. (2013), Alchalbi et al. (2009), Reilinger et al. (2006) and Özdemir *et al.* (2006) CORS (Turkey) stations. Black lines show the active fault line (fault map is taken from Emre et al. (2013).

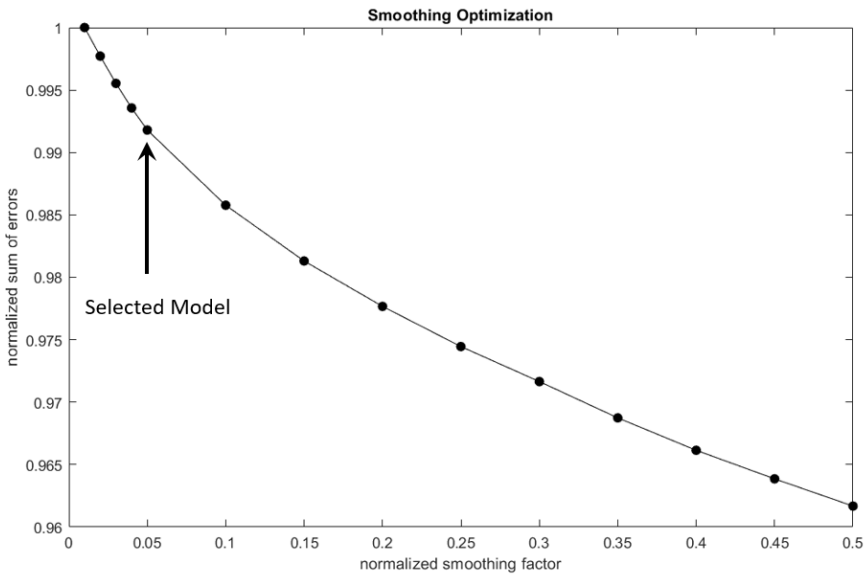

Figure 3.2: Smoothing factor optimization.

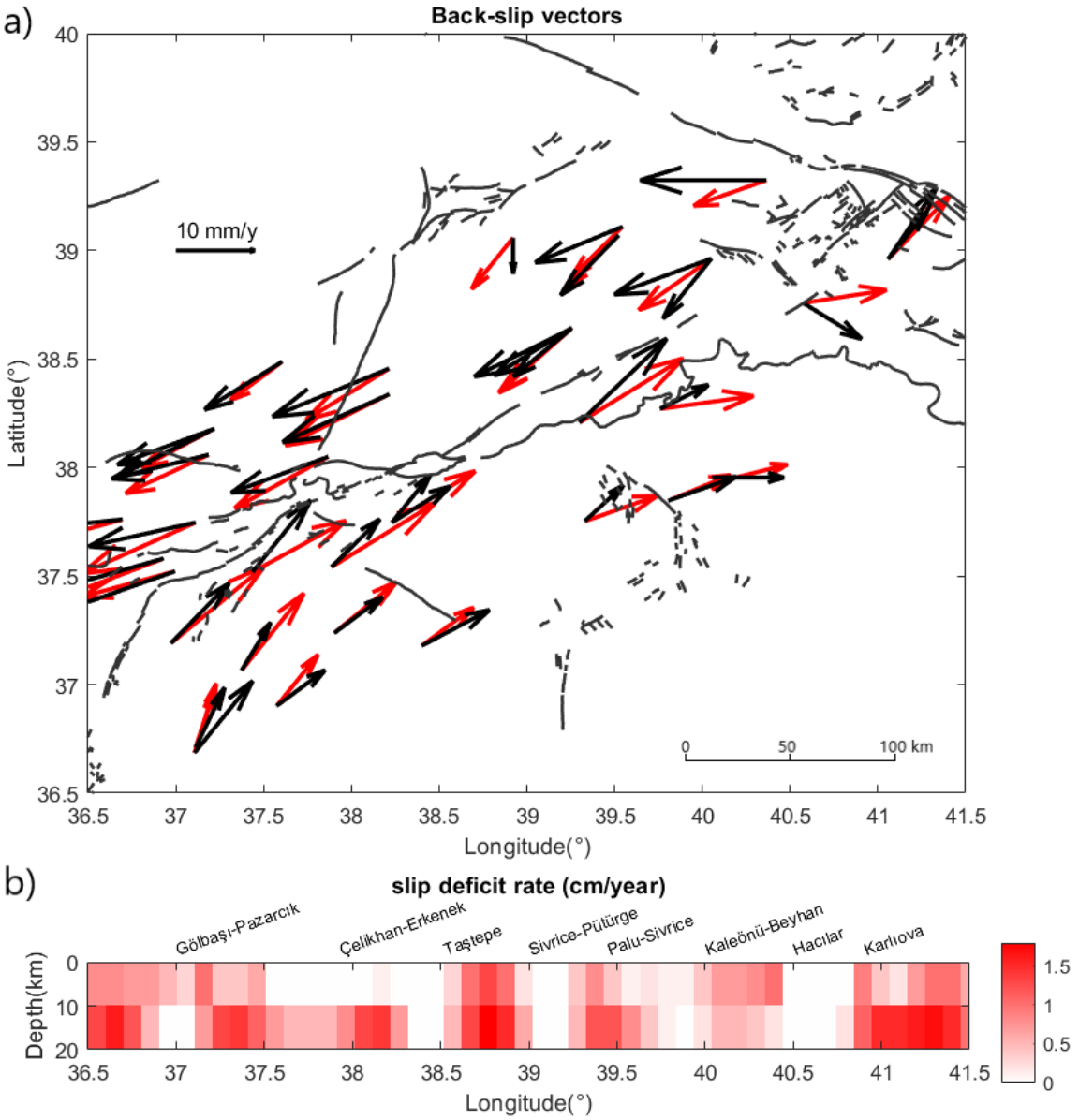

Figure 3.3: a) Observed and modelled back-slip data are shown with black and red vectors, respectively. Black lines are the active fault lines from Emre et al. (2013). b) Annual slip deficit rate model.

Since fault zone do not have a homogenous geometry, slip deficit rate can change from segment to segment. Average annual slip deficit is highest in the Palu-Sivrice segment with 11.4 mm/y, while the lowest is Hacılar segment with 0 mm/y. This also causes segments to have different earthquake generation cycles. For example, Kaleönü-Beyhan segment has a slip deficit rate of 0.7 mm/y and has not ruptured over 1000 years. On the other hand, Sivrice-Pütürge segment generated a major earthquake after 145 years with the slip deficit rate of 4 mm/y.

On the Karlıova segment the average annual slip deficit is 9 mm/y. Slip deficit is accumulated between 10 and 20 km depth. On the other hand, the Hacılar segment does not show any accumulation of slip deficit. The Kaleönü-Beyhan segment has an annual slip deficit of 0.7 mm/y. Slip deficit on this segment is mostly observed 0 to 10 km depth. The Palu-Sivrice segment has an annual slip rate of 11 mm/y. The slip deficit is observed between 10 and 20 km depth. The Sivrice-Pütürge segment has an annual slip deficit rate of 4 mm/y. Also, the slip deficit is mostly observed between the same depth as the Palu-Sivrice segment. Taştepe segment being the shortest segment, has an annual slip rate of 11 mm/y and has the highest slip deficit patch of 18 mm/y. Slip deficit is observed between same depth as the prior segment. The Çelikhan-Erkenek segment has an annual slip rate of 6 mm/y. the Slip deficit is observed mostly between 10 and 20 km depth. The Gölbaşı-Pazarcık segment has an annual slip rate of 4 mm/y. This segment is the longest segment of the EAFZ and the slip deficit shows a non-homogenous distribution. On the general, segments slip deficit is observed on the western patches of the segments.

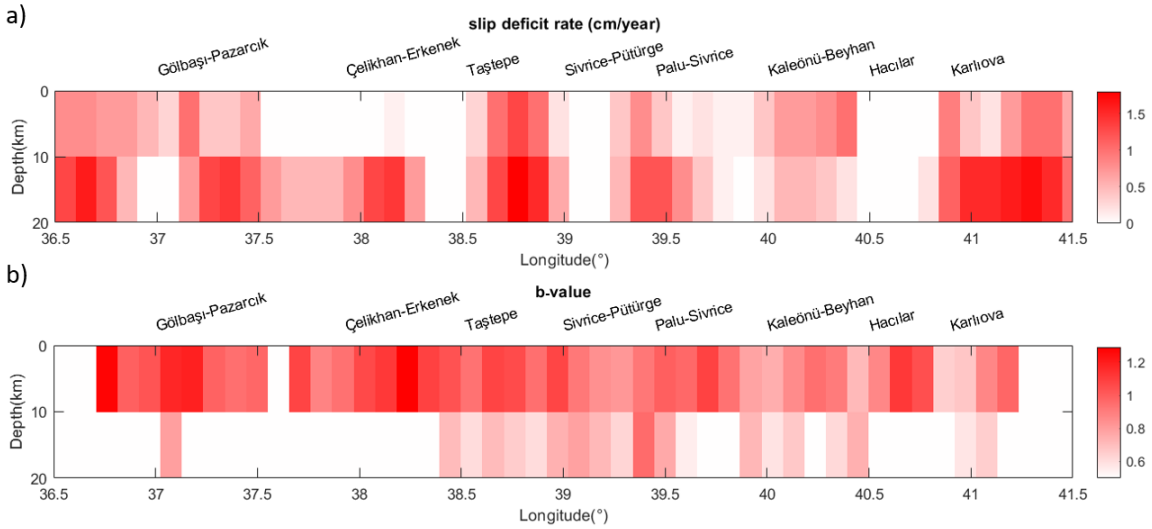

Figure 3.4: a) Annual slip deficit rate model. b) b-value model along the fault line.

Slip deficit rate and b-value are compared in Figure 3.4. b-value increases with the increasing seismicity, while slip deficit decreases at the same time. Overall pattern is that the slip deficit and b-value are inversely correlated. b-value is high on the patches with low slip deficit. High b-value near the surface indicates that there are shallow earthquakes along the EAFZ.

Segment-by-segment comparison between slip deficit and b-value is as follows:

(1) The Karlıova segment, the north-easternmost section of the EAFZ, hosts the lowest b-value. There, the high slip deficit rate and low b-value are observed at the depth range of 10-20 km (Figure 3.4).

(2) The Hacılar segment has entirely a low slip deficit rate between surface and 20 km depth. The segment has low b-value between 10-20 km depth and has a b-value around 1.0 between surface and 10 km depth. The low slip deficit rate and low b-value between 10-20 km depth does not suggest any inverse correlation.

(3) The Kaleönü-Beyhan segment has a relatively higher slip rate than the Hacılar segment and has a lower b-value between 10-20 km depth.

(4) Along the Palu-Sivrice segment, slip deficit rates are high towards the south-west and at depth. The segment has a low b value between 10-20 km depth, which shows a reverse correlation with slip deficit and therefore can indicate a fault below 10 km.

(5) The slip deficit rate is high at the southern section of the Sivrice-Pütürge segment. The b-value is around 1.0 at the northern patches of the segment. Deeper patches in the southwest host higher b-values and slip deficit rates.

(6) The Taştepe segment has high slip deficit rates along the north-eastern patches. Slip deficit rates decreases towards the southwest. The segment has also low b-values at deeper patches.

(7) The Çelikhan-Erkenek segment has low slip deficit rate between the surface and 10 km depth and high b-values in the same region. At the lower patches of the segment there is high slip deficit and low b-values.

(8) The south-westernmost Gölbaşı-Pazarcık segment has a high slip deficit rate around the middle part of the segment. The b-values are low at deeper patches.

b-value plot examples are given in Figure 3.5. by using the data recorded from the EAFZ to demonstrate how the slope changes in the plot of frequency-magnitude distribution. Figure 3.5a. has a plot of high b-value and Figure 3.5b. has a plot of low b value. From the Figure 3.5, the effect of earthquakes with larger magnitudes can be seen.

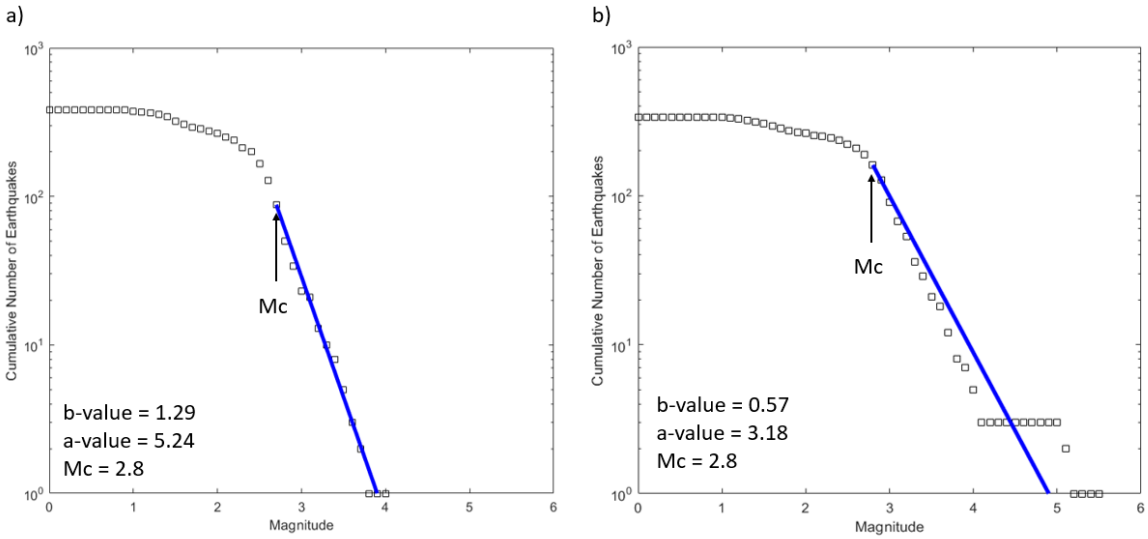

Figure 3.5: Examples of b-value graphics; a) High b-value graphic. b) Low b-value graphic. (The data used in creation of these graphics is from AFAD earthquake catalogue between 2005 and 2019.)

3.2. Current Earthquake Potential

At this point we can calculate the current earthquake potential by using Equations (2.8) and (2.9). We have all the elements to calculate the possible earthquake magnitude. Length, total slip deficit, last earthquake date and magnitude are given in the Table 3.1. Figure 3.6 also demonstrates the accumulated slip deficit of the segments from the latest failure of the segments till 2020. Highest slip accumulation occurred along the Kaleönü-Beyhan and Gölbaşı-Pazarcık segments, which lastly failed in 995 and 1513, respectively. The last column of the Table 3.1 lists our calculations for the current magnitude potential of the segments. The current magnitude potentials of the segments are also shown on the map in Figure 3.7.

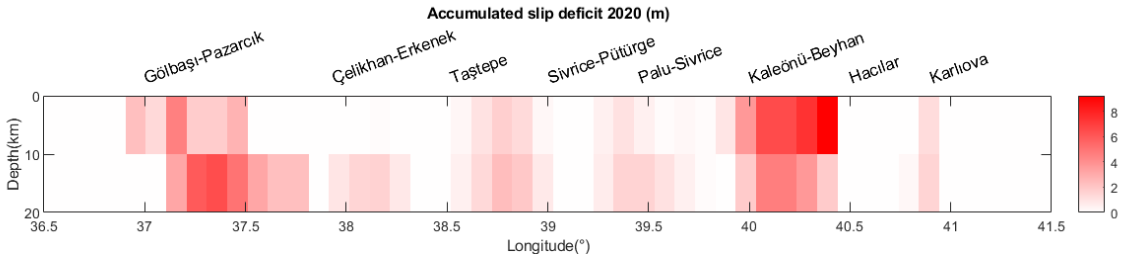

Figure 3.6: Accumulated total slip deficit from the latest failure of the segments.

On the Easternmost Karlıova segment, the last earthquake occurred in 1866 with a magnitude of 7.0. Since 1866 the segment has accumulated a total slip deficit of 145.5 cm, which can currently generate an earthquake with a magnitude of 7.0.

Hacılar segment has zero slip deficit and current magnitude potential cannot be calculated (Table 3.1). There can be two reasons for this result. First reason is, there is no accumulation due to strain energy being released through many minor earthquakes. Second reason is there is not enough length of data around the region to accurately determine slip deficit.

On the Kaleönü-Beyhan segment there is a total slip deficit of 73.5 cm. This slip deficit is accumulated over 1000 years since the last rupture occurred on this segment in 995. Currently the accumulated slip deficit can generate an earthquake with a magnitude of 6.9.

The Palu-Sivrice segment accumulated a total slip deficit of 167.6 cm since its last rupture in 1874. The segment currently has a magnitude potential of 7.1, which is the same as the last earthquake magnitude.

The Sivrice-Pütürge segment has accumulated 60.3 slip deficit since its last earthquake in 1875. In the last row of the table Sivrice-Pütürge segment is written again to demonstrate the forecasting. Magnitude potential of Sivrice-Pütürge segment quanti-

fied in this study perfectly correlates with the magnitude of the earthquake occurred on the same segment on January 24, 2020.

The Taştepe segment has not ruptured since 1905. From its last rupture segment accumulated a total slip deficit of 131.4 cm. Which has the current magnitude potential of 6.8. Current magnitude potential is the same as the earthquake magnitude occurred in 1905.

The Çelikhan-Erkenek segment has a total slip deficit of 77 cm. The last earthquake occurred on this segment in 1893. Currently, the segment has a magnitude potential of 6.9.

The highest magnitude potential is accumulated at the westernmost segment Gölbaşı-Pazarcık segment. This segment has not generated a major earthquake over 500 years. The segment has a low annual slip deficit rate, but like Kaleönü-Beyhan segment, since it has been accumulating strain energy for a long time it has a high magnitude potential of M 7.4.

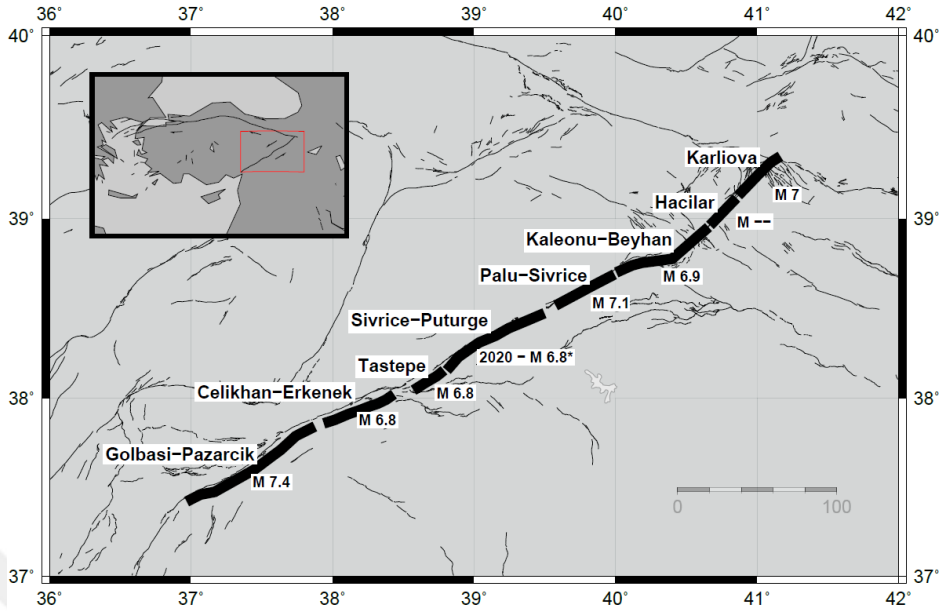

Figure 3.7: Current magnitude potentials of the segments are shown. (* Magnitude forecasting confirmed by the January 24, 2020 M 6.8 Earthquake; grey lines are active fault lines from Emre *et al.* (2013).)

Table 3.1: Segmentation, slip rates and latest failure of segments. (* Magnitude forecasting confirmed by the January 24, 2020 M 6.8 Earthquake.)

ID	Segment (Lat Lon, Lat Lon)	Length (km)	Annual Slip Deficit (cm/y)	Total Slip Deficit(cm)	Last Earthquake Date	Last Earthquake Magnitude	Current Magnitude Potential
Karlıova	39.11 40.87, 39.33 41.16	35	0.9	145.5	1866	7.0	7.0
Hacılar	38.95 40.66, 39.10 40.85	23	0	0	1971	6.8	-
Kaleönü-Beyhan	38.69 40.00, 38.94 40.65	65	0.1	73.5	995	7 < M <7.8	6.9
Palu-Sivrice	38.42 39.34, 38.69 39.98	64	1.1	167.6	1874	7.1	7.1
Sivrice-Pütürge	38.15 38.80, 38.42 39.32	55	0.4	60.3	1875	6.8	6.8
Taştepe	38.02 38.52, 38.15 38.78	23	1.1	131.4		6.8	6.8
Çelikhan-Erkenek	37.81 37.93, 38.04 38.43	47	0.6	77	1893	7.1	6.8

Table 3.1. Segmentation, slip rates and latest failure of segments. (* Magnitude forecasting confirmed by the January 24, 2020 M 6.8 Earthquake.) (cont.)

ID	Segment (Lat Lon, Lat Lon)	Length (km)	Annual Slip Deficit (cm/y)	Total Slip Deficit(cm)	Last Earthquake Date	Last Earthquake Magnitude	Current Magnitude Potential
Gölbaşı-Pazarcık	37.44 36.90, 37.84 37.87	92	0.4	245.5	1513	7.4	7.4
Sivrice-Pütürge	38.15 38.80, 38.42 39.32	55	-	60.3	2020*		6.8

4. DISCUSSION

Our calculations for earthquake potential along the EAF strongly depend on locations and times of historical earthquakes, segmentation of the fault zone, and its present day slip budget. Therefore, we carefully consider reliabilities of all these parameters.

4.1. Historical Earthquakes and Segmentation

Historical earthquake catalogue is compiled from previous studies. It is the only data to represent latest failure of the fault segments. Historical earthquakes are also used to confirm segmentation of the fault zone integrating them with structural investigations. We reviewed all geological and seismological studies investigating historical earthquakes along the EAFZ (Ambraseys, 1971; Ambraseys, 1988; Barka & Kadinsky-Cade, 1988; Şaroğlu *et al.*, 1992; Ambraseys & Jackson, 1998; Ambraseys, 2001; Nalbant *et al.*, 2002; Herece, 2008; Grünthal & Wahlström, 2012; Duman & Emre, 2013 and KOERI earthquake catalogue). There, earthquakes are included only if they are verified by different studies. Temporal variation of earthquake magnitudes indicates that M 6.5+ earthquakes are completely included in our catalogue for the time period of 1000 - 2000 (Figure 4.1).

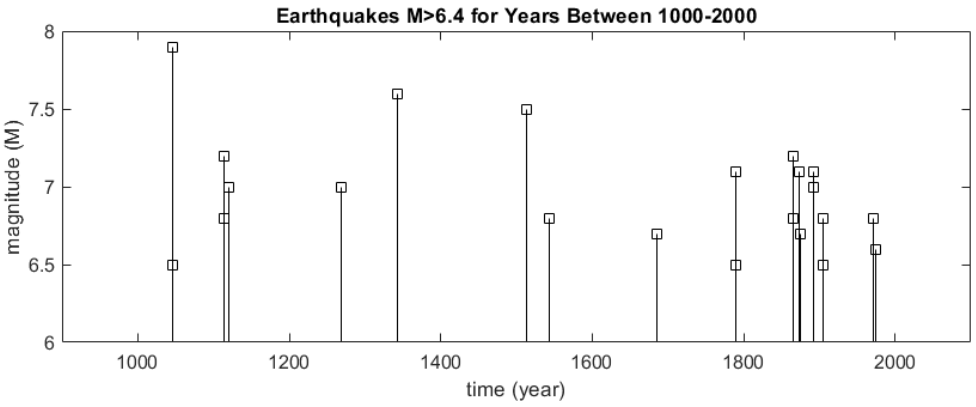

Figure 4.1: Temporal variation of magnitude for M 6.5+ earthquakes for the time period of 1000-2000. Also shown in Table 1.1.

Ambraseys (1988) suggested three segments along the section from Karlıova to Antakya. However, even the middle segment between Gölbaşı and Pütürge generated four strong/major earthquakes during the last cycle (M 7.1 in 1874, M 6.8 in 1875, M 7.1 in 1893, M 6.8 in 1905) (Figure 1.3, Table 3.1). In this context, the EAFZ must have a more complicated segmentation.

Barka & Kadinsky-Cade (1988), proposed fourteen segments based on structural variations along the EAFZ. Similarly, Herece (2008) suggested eleven segments along the EAFZ. However, the segments are too short to generate past strong/major earthquakes that are reported in the historical catalogue. For example, the 1513 M 7.4 Gölbaşı-Pazarcık earthquake generated a single rupture along a ∼92 km section of the EAFZ, which was however split into four sub segments by Barka & Kadinsky-Cade (1988) (Figure 1.3).

Şaroğlu *et al.* (1992) suggested six segments along the EAFZ between the Karlıova and Antakya based on step overs and changes in fault strike. However, magnitudes and locations of historical earthquakes are not fully compatible with this segmentation. There are eight strong/major earthquakes in the last cycle suggesting eight segments between Karlıova and Türkoğlu segments (Figure 1.3, Table 3.1). According to Şaroğlu *et al.* (1992), there are two fault segments that should fail twice in an unreasonably short time within the same cycle. This contradicts with the historical earthquake catalogue.

Nalbant *et al.* (2002) divided the EAFZ into eight segments to investigate history of stress change. This segmentation is similar to the segmentation we suggest, except for the Kaleönü-Beyhan, Palu-Sivrice and Sivrice-Pütürge segments. There, the 1874 (M 7.1) rupture was extended towards the Kaleönü-Beyhan segment although we interpret that it activated only Palu-Sivrice segment. Furthermore, the 1875 must have ruptured entire Sivrice-Pütürge segment to generate M 6.8 (Figure 1.3). However, Nalbant *et al.* (2002) assigned a much smaller section to this event.

Duman and Emre (2013) divided the main strand of the EAFZ into seven segments and six fault jog structures. Unlike our segmentation, Duman & Emre (2013) includes the Amanos region into the main strand of the EAFZ. However, we excluded the Amanos region from the fault zone in order to exclude the DSF in our calculations. Our segmentation and the segmentation by Duman and Emre are similar from the Karlıova to the Türkoğlu segment. Although the segmentations are similar, the segmentation by Duman and Emre has very long segment overlaps. Our segmentation model is based on ruptures of the historical earthquakes (MTA, 1992) to eliminate overlapping segments. Otherwise, overlapping segments will artificially overestimate magnitude forecasts.

Based on our review, we suggest eight fault segments along the EAFZ (Ambraseys, 1988; Barka & Kadinsky-Cade, 1988; Şaroğlu *et al.*, 1992; Ambraseys & Jackson, 1998; Nalbant *et al.*, 2002; Herece, 2008; Duman & Emre, 2013). The segmentation is based on the geometry of the fault segments obtained from previous studies and ruptures generated by historical earthquakes. Our slip deficit calculations verify this segmentation with high/low slip deficit rates at different fault segments.

4.2. Slip Deficit Release and Locking Depth

Eight segmented model along the EAFZ is in consistence with the along fault distribution of slip deficit rates (Figure 3.3). Transitions between high and low slip deficit rates along the EAFZ are in good agreement with the segment boundaries.

Based on the average slip rate of ∼10 mm/y (Aktuğ et al. 2016), the EAFZ should have accumulated totally 10.00 m slip on average during the last millennia. Historical earthquakes released 8.49 m of this slip accumulation and therefore left an average slip deficit of 1.51 m (Figure 4.2). Based on GPS-derived back-slips, average slip deficit along the EAFZ should be currently 1.50 m (Figure 3.5). This almost perfect agreement between seismicity derived and GPS derived slip deficits confirm that the EAFZ has presently 1.50 m slip deficit to be released by the future earthquakes.

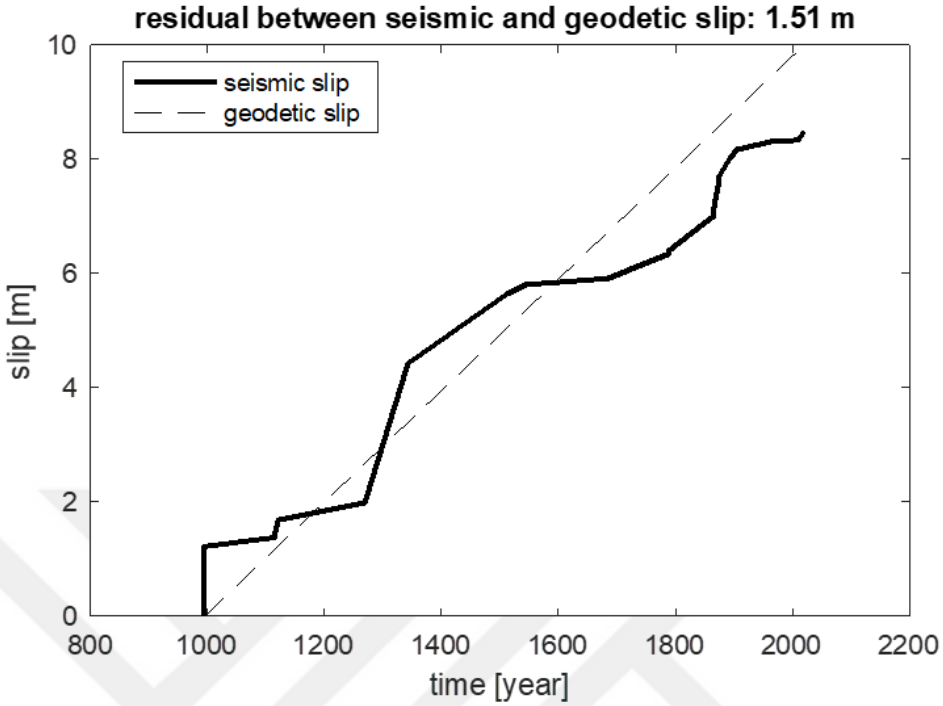

Figure 4.2: Comparison between seismic and geodetic slip during the last millennia.

Cavalie & Johnson (2014), Walters *et al.* (2014) used InSAR to identify a slip rate and locking depths along the EAFZ. Cavalie & Johnson (2014) defines a slip rate of 13.0 mm/y and a locking depth of 4.5 km from the Karlıova to the Sivrice-Pütürge segments, while Walters *et al.* (2014) define an average slip rate of 11.0 ± 3 mm/y and an average locking depth of 15 ± 5 km from the Karlıova to the southwest of the Gölbaşı-Pazarcık segment. Aktuğ *et al.* (2016) characterized slip rates and locking depths using a dense GPS velocity field. They reported a slip rate of 11.1 ± 3.9 mm/y and a locking depth of 12 km along the north-eastern segments (from Taştepe to Kaleönü-Beyhan), and a slip rate of 10.7 ± 0.9 mm/y and a locking depth of 25 km along the south-western segments (from Gölbaşı-Pazarcık to Çelikhan-Erkenek).

In this study, we projected GPS measurement onto fault plane to investigate distribution of slip deficit rates along the fault zone patch by patch (Figure 3.3) rather than one dimensional arctangent modelling. Arctangent approach makes an overall approximation for the entire segment while our slip inversion focuses on each 10x10

km patches on the fault plane. According to Cavalie & Johnson (2014) locking depth is 4.5 km along the section from Karlıova to Pütürge. This suggests that 22.5% of the total slip rate and therefore 2.9 mm/y is annually accumulated as slip deficit. Along this section, our calculations show an average slip deficit of 5.3 mm/yr. Locking depth along the section from Karlıova to the southwest of the Gölbaşı-Pazarcık segment is 15.0 km according to Walters *et al.*, 2014 suggesting that 75% of the total slip rate and therefore 8.2 mm/y is annually accumulated. Along this section, Aktuğ *et al.*, 2016 suggested 12 km locking depth corresponding to 6.6 mm/y slip deficit rate. In this study, we found an average slip deficit rate of 5.8 mm/y along this section of the EAFZ. Although our results converge results from the previous studies up to 88%, mismatches may result in significant changes in slip forecasts for future earthquakes.

4.3. B-value and Slip Deficit Distribution

Comparing along-fault distribution of slip deficit rate and b-value, we elaborate on whether b-value might be used to differentiate locked and creeping fault segments. In general, slip-deficit rates are reversely correlated with b-values except for the Hacılar segment (Figure 3.3).

Scholz (1968) had previously suggested that low b-value is an indication of high stress, and vice versa. Wyss (2001) observed low b-values down to 0.5 at locked fault patches and high b-values up to 1.3 along at creeping fault patches. However, Goebel *et al.* (2017) observed in laboratory experiments that, low b-values ranging from 0.6 to 0.7 are hosted along smooth surfaces, while high b-values ranging from 1.2 to 1.3 are hosted along rough and highly fractured surfaces. We anticipate that smooth fault surfaces host lower friction and therefore lower coupling compared to rough and highly fractured fault surfaces (Scholz, 2019).

In this context, reverse correlation, which we observe between slip deficit rates and b-values, confirms rather Scholz (1968) and Wyss (2001). According to our observations, low b-values identify high slip deficit rates and therefore locate highly stressed

locked fault patches. On the other hand, high b-values identify low slip deficit rates and therefore locate lowly stressed creeping fault patches.

4.4. January 24, 2020 Elazığ Earthquake

The January 24 M 6.8 2020 Elazığ earthquake ruptured the Sivrice-Pütürge segment of the EAFZ. The main shock hypocentre is located 38.3775°N, 39.1042°E and at 5.0 km depth (reported by KOERI). This event allowed us to test our idea to see whether our magnitude forecast approach works properly. In our results, there are two prominent slip deficit patches near the main shock hypocentre. Average slip deficit rate is 0.4 cm/y and therefore total slip accumulation since the 1875 M 6.8 earthquake is of 60.3 cm. This slip deficit has a potential to generate a Mw 6.8 earthquake, exactly the observed magnitude of the 2020 event.

Along the Sivrice-Pütürge segment, we observe that the 2020 rupture perfectly match with the 1875 earthquake failing the same segment and generating the same earthquake magnitude. The 2020 Elazığ aftershocks are distributed mainly along the Sivrice-Pütürge segment (Figure 4.3). In this context, the segmentation we suggest in this study is verified by the magnitude of the main shock as well as the aftershock distribution. In conclusion, the magnitude forecasting approach used in this study is well confirmed by the 2020 Elazığ earthquake.

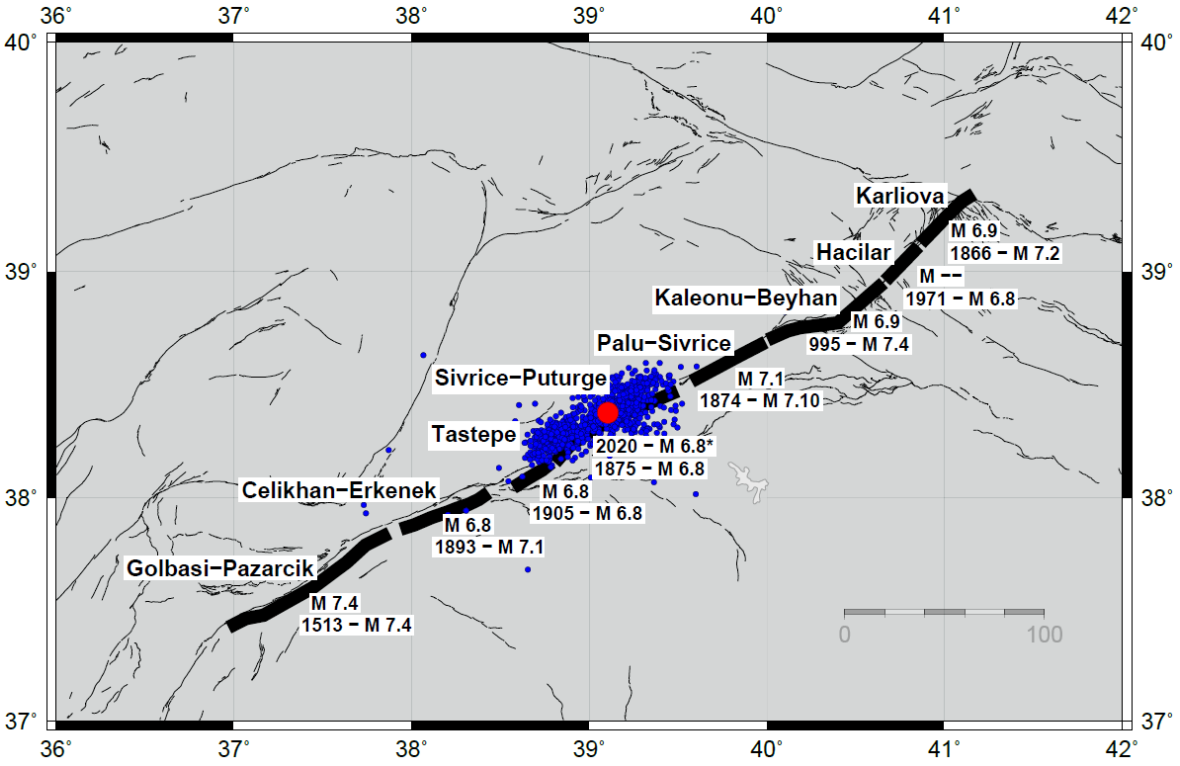

Figure 4.3: Along fault distribution of January 24th, 2020 Elazığ earthquake and aftershocks. The red dot indicates epicentre of the M 6.8 main shock and blue dots indicate epicentres of the aftershocks (KOERI). Bold black line shows segments of the EAFZ we suggested in this study. Current magnitude potentials and latest rupture dates of the segments are shown. The thin black lines are the active fault lines taken from Emre et al. (2013).

5. CONCLUSION

GPS-derived slip deficit rates indicate that the EAFZ currently host a 1.51 m average slip deficit to be released by the future earthquakes. This is almost perfectly verified by historical earthquakes indicating currently a 1.50 average slip deficit along the EAFZ.

The EAFZ consists of eight fault segments generating quasi-periodic strong and major earthquakes depending on their dimensions as well as slip deficit budgets.

One of these segments has failed recently on January 24, 2020, and verified our interpretation for segmentation as well as magnitude forecast. 60.3 cm slip deficit since the 1875 M 6.8 earthquake (slip deficit of 145 years) generated a M 6.8 on January 24, 2020 failing the same segment.

The Hacılar segment does not accumulate slip deficit due to its low coupling. Remaining six segments have potential to generate three strong as well as three major earthquakes.

The Karlıova segment has currently potential to generate a M 7.0 earthquake. The Kaleönü-Beyhan segment has currently potential to generate a M 6.9 earthquake. The Palu-Sivrice segment has currently potential to generate a M 7.1 earthquake. The Taştepe segment has currently potential to generate a M 6.8 earthquake. The Çelikhan-Erkenek segment has currently potential to generate a M 6.9 earthquake. The Gölbaşı-Pazarcık segment has currently potential to generate a M 7.4 earthquake. Four of these segments (Karlıova, Palu-Sivrice, Taştepe, Gölbaşı-Pazarcık) have accumulated slip deficits enough to generate magnitudes of earthquakes they generated in previous cycle.

Our observations verified that b-value can be used to differentiate between locked

and creeping fault segments based on reverse correlation between slip deficit rate and b-value distribution along the EAFZ.

In summary, although earthquakes are not time predictable, forecasting location and size of future strong/major earthquakes might be possible if historical records of earthquakes and geodetic infrastructure are sufficiently available.

REFERENCES

1. Aki, K., "Maximum likelihood estimate of b in the formula log N= a-bM and its confidence limits", *Bull. Earthq. Res. Inst., Tokyo Univ.*, Vol. 43, pp. 237–239, 1965.

2. Aktug, B., J. Nocquet, A. Cingöz, B. Parsons, Y. Erkan, P. England, O. Lenk, M. Gürdal, A. Kılıcoglu, H. Akdeniz *et al.*, "Deformation of western Turkey from a combination of permanent and campaign GPS data: Limits to block-like behavior", *Journal of Geophysical Research: Solid Earth*, Vol. 114, No. B10, 2009.

3. Aktug, B., E. Parmaksız, M. Kurt, O. Lenk, A. Kılıcoglu, M. A. Gürdal and S. Ozdemir, "Deformation of central anatolia: GPS implications", *Journal of Geodynamics*, Vol. 67, pp. 78–96, 2013.

4. Aktug, B., H. Ozener, A. Dogru, A. Sabuncu, B. Turgut, K. Halicioglu, O. Yilmaz and E. Havazli, "Slip rates and seismic potential on the East Anatolian Fault System using an improved GPS velocity field", *Journal of Geodynamics*, Vol. 94-95, pp. 1–12, 01 2016.

5. Alchalbi, A., M. Daoud, F. Gomez, S. McClusky, R. Reilinger, M. A. Romeyeh, A. Alsouod, R. Yassminh, B. Ballani, R. Darawcheh *et al.*, "Crustal deformation in northwestern Arabia from GPS measurements in Syria: Slow slip rate along the northern Dead Sea Fault", *Geophysical Journal International*, Vol. 180, No. 1, pp. 125–135, 2010.

6. Allen, C. R., "Active faulting in northern Turkey", , 1969.

7. Ambraseys, N. N., "Value of historical records of earthquakes", *Nature*, Vol. 232, No. 5310, p. 375—379, August 1971, `https://doi.org/10.1038/232375a0`.

8. Ambraseys, N. N., "Engineering seismology: part II", *Earthquake engineering &*

structural dynamics, Vol. 17, No. 1, pp. 51–105, 1988.

9. Ambraseys, N. N., "Temporary seismic quiescence: SE Turkey", *Geophysical Journal International*, Vol. 96, No. 2, pp. 311–331, 1989.

10. Ambraseys, N. N., "Reassessment of earthquakes, 1900–1999, in the Eastern Mediterranean and the Middle East", *Geophysical Journal International*, Vol. 145, No. 2, pp. 471–485, 2001.

11. Ambraseys, N. N. and J. A. Jackson, "Faulting associated with historical and recent earthquakes in the Eastern Mediterranean region", *Geophysical Journal International*, Vol. 133, No. 2, pp. 390–406, 05 1998, https://doi.org/10.1046/j.1365-246X.1998.00508.x.

12. Arpat, E. and F. Şaroğlu, "The East Anatolian fault system; thoughts on its development", *Maden Tetkik ve Arama Dergisi*, Vol. 78, No. 78, pp. 1–12, 1972.

13. Barka, A. and K. Kadinsky-Cade, "Strike-slip fault geometry in Turkey and its influence on earthquake activity", *Tectonics*, Vol. 7, No. 3, pp. 663–684, 1988.

14. Bird, P., "AN updated digital model of plate boundaries", *Geochemistry Geophysics Geosystems*, Vol. 4, p. 1027, 03 2003.

15. *Boğaziçi University Kandilli Observatory Earthquake Research Institute, BDTIM Earthquake Query System*, 2020, http://www.koeri.boun.edu.tr/sismo/zeqdb/.

16. Bozkurt, E., "Neotectonics of Turkey", *Geodinamica Acta*, Vol. 14, pp. 3–30, 05 2001.

17. Bulut, F., M. Bohnhoff, T. Eken, C. Janssen, T. Kılıç and G. Dresen, "The East Anatolian Fault Zone: Seismotectonic setting and spatiotemporal characteristics of seismicity based on precise earthquake locations",

Journal of Geophysical Research: Solid Earth, Vol. 117, No. B7, 2012, https://agupubs.onlinelibrary.wiley.com/doi/abs/10.1029/2011JB008966.

18. Bulut, F., B. Aktug, C. Yaltırak, A. Dogru and H. Ozener, "Magnitudes of future large earthquakes near Istanbul quantified from 1500 years of historical earthquakes, present-day microseismicity and GPS slip rates", *Tectonophysics*, Vol. 764, pp. 77–87, 2019.

19. Cavalie, O. and S. Jonsson, "Block-like plate movements in eastern Anatolia observed by InSAR", *Geophysical Research Letters*, Vol. 41, No. 1, pp. 26–31, 2014.

20. Cetin, H., H. Güneyli and L. Mayer, "Paleoseismology of the Palu–Lake Hazar segment of the East Anatolian Fault Zone, Turkey", *Tectonophysics*, Vol. 374, No. 3, pp. 163 – 197, 2003, http://www.sciencedirect.com/science/article/pii/S0040195103003627.

21. Cox, A. and R. Hart, "Plate tectonics: How its works", *Palo Alto: Blackwell Sci. Pub*, 1986.

22. Davies, G. F. and M. A. Richards, "Mantle convection", *The Journal of Geology*, Vol. 100, No. 2, pp. 151–206, 1992.

23. Delph, J. R., G. Zandt and S. L. Beck, "A new approach to obtaining a 3D shear wave velocity model of the crust and upper mantle: An application to eastern Turkey", *Tectonophysics*, Vol. 665, pp. 92 – 100, 2015, http://www.sciencedirect.com/science/article/pii/S0040195115005326.

24. Dewey, J. F. and A. M. C. Şengör, "Aegean and surrounding regions: Complex multiplate and continuum tectonics in a convergent zone", *GSA Bulletin*, Vol. 90, No. 1, pp. 84–92, 01 1979, https://doi.org/10.1130/0016-7606(1979)90<84:AASRCM>2.0.CO;2.

25. *Disaster Emergency Management Authority Presidential of Earthquake Depart-*

ment, Earthquake Database, 2020, `https://deprem.afad.gov.tr/ddakatalogu`.

26. Duman, T. Y. and O. Emre, "The East Anatolian Fault: geometry, segmentation and jog characteristics", *Geological Society, London, Special Publications*, Vol. 372, No. 1, pp. 495–529, 2013.

27. Emre, O., T. Y. Duman, S. Ozalp, H. Elmacı, S. Olgun and F. Şaroğlu, "Mart 2010 Başyurt-Karakoçan (Elazığ) Depremi Değerlendirme Raporu", *MTA Jeoloji Etütler Dairesi*, 2010.

28. Emre, O., T. Y. Duman, S. Özalp, F. Şaroğlu, S. Olgun and H. Elmacı, "Active Fault Map of Turkey with an explanatory text 1:1,250,000 scale", *General Directorate of Mineral Research and Exploration, Special Publication Series*, Vol. 30, 2013.

29. Goebel, T. H. W., G. Kwiatek, T. W. Becker, E. E. Brodsky and G. Dresen, "What allows seismic events to grow big?: Insights from b-value and fault roughness analysis in laboratory stick-slip experiments", *Geology*, Vol. 45, No. 9, pp. 815–818, 2017.

30. Gutenberg, B. and C. F. Richter, "Earthquake magnitude, intensity, energy, and acceleration: (Second paper)", *Bulletin of the seismological society of America*, Vol. 46, No. 2, pp. 105–145, 1956.

31. Grünthal, G. and R. Wahlström, "The European-Mediterranean earthquake catalogue (EMEC) for the last millennium", *Journal of Seismology*, Vol. 16, No. 3, pp. 535–570, 2012.

32. Hanks, T. C. and D. M. Boore, "Moment-magnitude relations in theory and practice", *Journal of Geophysical Research: Solid Earth*, Vol. 89, No. B7, pp. 6229–6235, 1984.

33. Hanks, T. C. and H. Kanamori, "A moment magnitude scale", *Journal of Geo-*

physical Research: Solid Earth, Vol. 84, No. B5, pp. 2348–2350, 1979.

34. Hempton, M., J. F. Dewey and F. Şaroğlu, "The East Anatolian transform fault: along strike variations in geometry and behavior", *EOS Trans.*, Vol. 62, p. 393, 1981.

35. Herece, E. I. and E. Akay, *Doğu Anadolu fayı (DAF) atlası*, Maden Tetkik Arama Genel Müdürlüğü, 2008.

36. Jackson, J. and D. McKenzie, "The relationship between plate motions and seismic moment tensors, and the rates of active deformation in the Mediterranean and Middle East", *Geophysical Journal International*, Vol. 93, No. 1, pp. 45–73, 04 1988, https://doi.org/10.1111/j.1365-246X.1988.tb01387.x.

37. Kelley, H. J., "Method of gradients", *Mathematics in Science and Engineering*, Vol. 5, pp. 205–254, Elsevier, 1962.

38. Lutgens, F. K. and E. J. Tarbuck, *Earth: an introduction to physical geology*, Pearson Higher Ed, 2016.

39. Mignan, A. and J. Woessner, "Estimating the magnitude of completeness for earthquake catalogs", *Community Online Resource for Statistical Seismicity Analysis*, pp. 1–45, 2012.

40. Nalbant, S., J. McCloskey, S. Steacy and A. Barka, "Stress accumulation and increased seismic risk in Eastern Turkey", *Earth and Planetary Science Letters*, Vol. 195, pp. 291–298, 02 2002.

41. Nocquet, J.-M., "Present-day kinematics of the Mediterranean: A comprehensive overview of GPS results", *Tectonophysics*, Vol. 579, pp. 220–242, 2012.

42. Okada, Y., "Surface deformation due to shear and tensile faults in a half-space", *Bulletin of the seismological society of America*, Vol. 75, No. 4, pp. 1135–1154,

1985.

43. Okal, E. A. and B. A. Romanowicz, "On the variation of b-values with earthquake size", *Physics of the Earth and Planetary Interiors*, Vol. 87, No. 1-2, pp. 55–76, 1994.

44. Özdemir, S., H. Komutanlığı, J. Başkanlığı and Ankara, "TUSAGA ve TUSAGA-Aktif İstasyonlarının Hassas Koordinat ve Hızlarının Hesaplanması Üzerine (On the Estimation of Precise Coordinates and Velocities of TNPGN and TNPGN-Active Stations)", *Harita Dergisi*, Vol. 155, pp. 53–81, 01 2016.

45. Reid, H. F., "The mechanics of the earthquake", *The California Earthquake of April 18, 1906, Report of the State Earthquake Investigation Commission*, 1910.

46. Reilinger, R. E., S. C. McClusky, M. B. Oral, R. W. King, M. N. Toksoz, A. A. Barka, I. Kinik, O. Lenk and I. Sanli, "Global Positioning System measurements of present-day crustal movements in the Arabia-Africa-Eurasia plate collision zone", *Journal of Geophysical Research: Solid Earth*, Vol. 102, No. B5, pp. 9983–9999, 1997, https://agupubs.onlinelibrary.wiley.com/doi/abs/10.1029/96JB03736.

47. Reilinger, R., S. McClusky, P. Vernant, S. Lawrence, S. Ergintav and R. Cakmak, "GPS constraints on continental deformation in the Africa-Arabia-Eurasia continental collision zone and implications for the dynamics of the plate interactions", *J. Geophys. Res*, Vol. 111, 2006.

48. Royden, L. H., "Evolution of retreating subduction boundaries formed during continental collision", *Tectonics*, Vol. 12, No. 3, pp. 629–638, 1993.

49. Savage, J. C., "A dislocation model of strain accumulation and release at a subduction zone", *Journal of Geophysical Research: Solid Earth*, Vol. 88, No. B6, pp. 4984–4996, 1983.

50. Scholz, C. H., "Experimental study of the fracturing process in brittle rock", *Journal of Geophysical Research*, Vol. 73, No. 4, pp. 1447–1454, 1968.

51. Scholz, C. H., "The Mechanics of Earthquakes and Faulting. Cambridge University Press, Cambridge, 471 p", , 2002.

52. Scholz, C. H., *The mechanics of earthquakes and faulting*, Cambridge university press, 2019.

53. Shimazaki, K. and T. Nakata, "Time-predictable recurrence model for large earthquakes", *Geophysical Research Letters*, Vol. 7, No. 4, pp. 279–282, 1980.

54. Stern, R. J., "Subduction zones", *Reviews of geophysics*, Vol. 40, No. 4, pp. 3–1, 2002.

55. Şaroğlu, F., O. Emre and I. Kuşçu, "Active Fault Map of Turkey.", , 1992, Ankara-Turkey.

56. Şengör, A. M. C., "The North Anatolian transform fault: its age, offset and tectonic significance", *Journal of the Geological Society*, Vol. 136, No. 3, pp. 269–282, 1979, `https://jgs.lyellcollection.org/content/136/3/269`.

57. Şengor, A. M. C. and Y. Yilmaz, "Tethyan evolution of Turkey: A plate tectonic approach", *Tectonophysics*, Vol. 75, pp. 181–190, 06 1981.

58. Tsang, L., J. A. Kong, K.-H. Ding and C. O. Ao, *Scattering of electromagnetic waves: numerical simulations*, Vol. 25, John Wiley & Sons, 2004.

59. Walters, R., B. Parsons and T. Wright, "Constraining crustal velocity fields with InSAR for Eastern Turkey: Limits to the block-like behavior of Eastern Anatolia", *Journal of Geophysical Research: Solid Earth*, Vol. 119, No. 6, pp. 5215–5234, 2014.

60. Wang, R., F. Lorenzo-Martin and F. Roth, "PSGRN/PSCMP—a new code for calculating co-and post-seismic deformation, geoid and gravity changes based on the viscoelastic-gravitational dislocation theory", *Computers & Geosciences*, Vol. 32, No. 4, pp. 527–541, 2006.

61. Wang, L., R. Wang, F. Roth, B. Enescu, S. Hainzl and S. Ergintav, "Afterslip and viscoelastic relaxation following the 1999 M 7.4 Izmit earthquake from GPS measurements", *Geophysical Journal International*, Vol. 178, No. 3, pp. 1220–1237, 2009.

62. Wyss, M., "Locked and creeping patches along the Hayward fault, California", *Geophysical Research Letters*, Vol. 28, No. 18, pp. 3537–3540, 2001.

63. Wyss, M., C. G. Sammis, R. M. Nadeau and S. Wiemer, "Fractal dimension and b-value on creeping and locked patches of the San Andreas fault near Parkfield, California", *Bulletin of the Seismological Society of America*, Vol. 94, No. 2, pp. 410–421, 2004.